Revision 1

Title: U, Th and K partitioning between metal, silicate and sulfide and implications for Mercury's structure, volatile content and radioactive heat production

Authors: **Asmaa Boujibar[1]*, Mya Habermann[2,3,4], Kevin Righter[1], D. Kent Ross[5,6],**

Kellye Pando[5], Minako Righter[7], Bethany A. Chidester[8], Lisa R. Danielson[5]

Affiliations:

[1]NASA Johnson Space Center, Houston, TX 77058, USA.

[2]Lunar and Planetary Institute, Houston, TX 77058, USA.

[3]HX5, NASA Johnson Space Center, Houston, TX 77058, USA.

[4]University of New Mexico, Dept. of Earth and Planetary Sciences, Albuquerque, NM 87131, USA.

[5]Jacobs, NASA Johnson Space Center, Houston, TX 77058, USA.

[6]UTEP-CASSMAR, El Paso TX 79968, USA.

[7]University of Houston, Dept. of Earth and Atmospheric Sciences, Houston, TX 77204, USA.

[8]University of Chicago, Dept. of the Geophysical Sciences, IL 60637, USA.

*Present address: Geophysical Laboratory, Carnegie Institution of Washington, 5251 Broad Branch Road NW, Washington, DC 20015, USA.

Correspondence to: aboujibar@carnegiescience.edu

Abstract

The distribution of heat-producing elements (HPE) potassium (K), uranium (U) and thorium

(Th) within planetary interiors has major implications for the thermal evolution of the

terrestrial planets and for the inventory of volatile elements in the inner Solar System. To

investigate the abundances of HPE in Mercury's interior, we conducted experiments at high

pressure and temperature (up to 5 GPa and 1900 °C) and reduced conditions (IW-1.8 to IW-

6.5) to determine U, Th and K partitioning between metal, silicate and sulfide ($D^{met/sil}$ and

$D^{sulf/sil}$). Our experimental data combined with those from the literature show that partitioning

into sulfide is more efficient than into metal and enhanced with decreasing FeO and

increasing O contents of the silicate and sulfide melts respectively. Also, at low oxygen

fugacity (log fO_2 < IW-5), U and Th are more efficiently partitioned into liquid iron metal and

sulfide than K. $D^{met/sil}$ for U, Th and K increases with decreasing oxygen fugacity, while

$D_U^{met/sil}$ and $D_K^{met/sil}$ increase when the metal is enriched and depleted in O or Si respectively.

We also used available data from the literature to constrain the concentrations of light

elements (Si, S, O and C) in Fe metal and sulfide. We provided chemical compositions of

Mercury's core after core segregation, for a range of fO_2 conditions during its differentiation.

For example, if Mercury differentiated at IW-5.5, its core would contain 49 wt% Si, 0.02 wt%

S and negligible C. Also if core-mantle separation happened at a fO_2 lower than IW-4, bulk

Mercury Fe/Si ratio is likely to be chondritic. We calculated concentrations of U, Th and K in

the Fe-rich core and possible sulfide layer of Mercury. Bulk Mercury K/U and K/Th were

calculated taking all U, Th and K reservoirs into account. Without any sulfide layer or if

Mercury's core segregated at a higher fO_2 than IW-4, bulk K/U and K/Th would be similar to

those measured on the surface, confirming more elevated volatile K concentration than

previously expected for Mercury. However, Mercury could fall on an overall volatile

depletion trend where K/U increases with the heliocentric distance, if core segregation

occurred near IW-5.5 or more reduced conditions and with a sulfide layer of at least 130 km thickness. In these conditions, bulk Mercury K/Th ratio is close to Venus' and Earth's values. Since U and Th become more chalcophile with decreasing oxygen fugacity, to a higher extent than K, it is likely that at a fO_2 close to or lower than IW-6, both K/U and K/Th become lower than values of the other terrestrial planets. Therefore, our results suggest that the elevated K/U and K/Th ratios of Mercury's surface should not be exclusively interpreted as the result of a volatile enrichment in Mercury, but could also indicate a sequestration of more U and Th than K in a hidden iron sulfide reservoir, possibly a layer present between the mantle and core. Hence, Mercury could be more depleted in volatiles than Mars with a K concentration similar or lower than the Earth's and Venus', suggesting a volatile depletion in the inner Solar System. In addition, we show that the presence of a sulfide layer formed between IW-4 and IW-5.5 decreases the total radioactive heat production of Mercury by up to 30%.

5

Introduction

K/Th and K/U ratios are common indicators of volatile depletion in terrestrial planets (e.g. McDonough et al., 1992; O'Neill and Palme, 1998; Wänke et al., 1973). K is moderately volatile while U and Th are refractory elements that fractionate in a similar way during magmatic differentiation processes. Therefore, these ratios are ideal for estimating volatile depletion, as they remain constant during global mantle differentiation. Several studies have recently proposed that U, Th and K become more siderophile and chalcophile (i.e. "metal- and sulfide- loving" respectively) under reducing conditions, and are consequently present in non-negligible levels in planetary cores (e.g. McCubbin et al., 2012). Therefore, core segregation may fractionate these heat-producing elements (HPE) so that surficial K/U and K/Th are no longer representative of the bulk planet. A precise knowledge of the partitioning of HPE between core and mantle is therefore essential when addressing volatile distribution in the Solar System, as well as radioactive heating of planetary interiors.

Volatile depletion in planetary and asteroidal material likely resulted from incomplete condensation of the nebula due to energetic electromagnetic radiation of the young hot Sun during its T-Tauri stage (Albarède, 2009) and due to devolatilization of ejecta during energetic impacts that produce high temperatures. Prior to the MErcury Surface, Space, ENvironment, GEochemistry, and Ranging (MESSENGER) mission to Mercury, K/U and K/Th were only documented for Earth, the Moon, Mars and Venus. Mercury was expected to be volatile-depleted in comparison to the other terrestrial planets, due to its lower heliocentric distance and even more depleted if it was involved in energetic impacts (McCubbin et al., 2012). However, MESSENGER Gamma Ray Spectrometer (GRS) measured higher than expected K/Th (5200 ±1800) and K/U (12800 ±4300) ratios with nearly Martian K/Th and terrestrial K/U values (Peplowski et al., 2011). These results were interpreted as evidence that Mercury is as volatile-rich as the other terrestrial planets, which challenges planetary

6

formation models. However, measurements of the Mercurian gravity field suggested the

presence of dense material above the Fe-rich core, which could represent an iron sulfide shell

(Hauck et al., 2013; Smith et al., 2012), formed due to the immiscibility between Si-rich and

S-rich Fe-alloys (e.g. Chabot et al., 2014; Malavergne et al., 2010). Because FeS could

incorporate HPE, the presence of this layer might complicate any interpretation of surficial

HPE ratios (McCubbin et al., 2012).

Resolution of the role of any sulfide layer in the distribution of HPE elements within

Mercury has been hindered by the sparse partitioning data at the pressure, temperature, fO_2,

and compositional conditions relevant to core formation. A number of studies explored the

change of HPE partitioning with different parameters, such as the effect of pressure and S-

content of metals on U partitioning (Blanchard et al., 2017; Chidester et al., 2017; Wohlers

and Wood, 2017), but there are nonetheless gaps in understanding the partitioning of all three

elements in both metal and sulfide-bearing systems. Therefore, we present experimental data

on U, Th and K partitioning between metal, silicate and sulfide at high pressure and

temperature, and combine them with previous work to derive predictive thermodynamic

models. Specifically, we address for the first time the effects of temperature, fO_2 and major

light elements present in planetary cores (S, Si, C and O) on U, Th and K partitioning, and

examine the implications for bulk K/U and K/Th ratios and volatile-content in Mercury.

Method

Starting compositions of experiments

Starting compositions consisted of 50 wt% silicate and 50 wt% metal powders. The bulk

compositions were chosen similar to EH4 enstatite chondrites (Berthet et al., 2009) (which are

the most reduced known chondrites) with a decreased concentration of O relative to EH4, in

order to reach a lower silicate/metal mass ratio of 50/50 close to Mercury's ratio. Sulfur and silicon in the metal phases were varied from 9-26 wt% S and 8-51 wt% Si. Addition of Si enabled partially control of the fO_2 to values intermediate between the IW and Si-SiO$_2$ buffers (see section 3.2). We used 3 silicate mixtures – one doped with 2.9 wt% UO$_2$ and 2.9 wt% ThO$_2$, and two doped with K (17 wt% K$_2$O) (Table 1).

The silicate phases were prepared by mixing dried ultra-pure SiO$_2$, MgO, Al$_2$O$_3$, TiO$_2$, Cr$_2$O$_3$, MnO$_2$, Na$_2$CO$_3$, CaCO$_3$, K$_2$CO$_3$, ThO$_2$ and depleted UO$_2$ powders under alcohol using an agate mortar and pestle. As UO$_2$ powder contains a small amount of polymer binder, it was initially washed in ethanol and heated at 100 ˚C prior to sample preparation. The silicate mix was then decarbonated overnight at 1073 K. Metals were prepared by mixing pure Fe, FeS, Ni, Co and Si. Metal and silicate powders were then intimately mixed together dry using an agate mortar and pestle.

Experimental methods

The experiments were conducted using 10 mm and 13 mm non end-loaded piston cylinder apparatuses (calibrated in (Filiberto et al., 2008)), and Walker-type multi anvil presses at NASA Johnson Space Center (calibrated in (Righter et al., 2008)), and at the Geophysical Laboratory (calibrated in (Bennett et al., 2016)). Experiments were conducted at pressures of 1 to 5 GPa, temperatures from 1500°C to 1900°C and at an fO_2 ranging between 1.8 and 6.5 log units below the iron-wustite buffer (Table 2). For all experiments, sample powders were loaded in graphite capsules and temperature was measured with a W/Re thermocouple. We used BaCO$_3$ as a pressure medium and graphite heaters for piston cylinder experiments and Re foil or graphite heaters for multi-anvil experiments. For experiments carried out using the multi anvil press, we used WC cubes of 8 mm truncated- edge length (TEL). Experiments were heated for 5 min to 3h30 (depending on the temperature, considering diffusion times of U and Th (la Tourrette and Wasserburg, 1997)) (Table 2) before their quench, then mounted in epoxy. The U-Th series of

8

samples were polished using methanol and Buehler diamond-polishing suspension paste while the K-series samples were dry polished using alumina and boron nitride powders, in order to avoid K loss in solutions.

Analytical methods

Prior to quantitative analysis, run products were characterized by BSE imaging using a JEOL LV-5910 and FEG 7600F scanning electron microscopes at NASA-JSC. Major, minor and trace elements including U, Th and K in sulfides were analyzed using electron microprobe analysis at NASA-JSC and the Carnegie Institution of Washington.

EMPA analysis utilized the FEG-JEOL 8530F and CAMECA SX100 electron microprobes at NASA JSC. Because of graphite capsule use, most metals contain carbon (up to 7 wt% C). O and C in metals and sulfides were analyzed at the JEOL JSM-6500F electron microscope, at the Carnegie Institution of Washington, using Fe_3O_4 and Fe_7C_3 standards respectively. Fe_7C_3 standard was synthesized at 14 GPa using multi anvil press (Liu et al., 2016). U and Th in silicates and sulfides were also analyzed using electron microprobe, as their concentrations were well above the detection limits (> 0.3 wt% while the detection limit was ~0.02 wt%). Analyses were performed with an accelerating voltage of 15 kV and a beam current of 15 nA for silicates and sulfides and 20 nA for metals. We used standards of pure metals, silicates, oxides and sulfides. For U and Th, standards of UO_2 and monazite were used. In order to encompass heterogeneous quench microstructures in metal and silicate melts, the electron beam was defocused to a circular spot of 5 to 30 μm. Positions of the peaks and backgrounds were chosen to avoid interferences: U Mα 1st order line - Fe Kα 2nd order line and Th Mα 1st order line - Fe Kα 2nd order line overlaps.

K in metals, sulfides and silicates was also measured using EPMA. Although K concentrations in metals are low, we were able to use electron microprobe to perform K measurement. We did not use laser ablation inductively coupled plasma mass spectrometry

9

(LA-ICP-MS) to measure trace K, as its mass is very close to that of Ar, which is the vaporizing and ionizing plasma in the LA-ICP-MS technique. Instead, after measuring major elements with EPMA in normal conditions (see above), we analyzed K in metals with an accelerating voltage of 15 kV and a beam current of 400 nA. Although alkalis are known to be mobile under high current in silicate glasses, it is not expected to be the case in metals. This was confirmed by the fact that K concentrations in metals at 400 nA were not lower than at 20 nA. Increasing the beam current allowed an increase of the number of counts and a decrease of the detection limit to 6 ppm K. We used orthoclase as a standard and time acquisition of 100 s on the peak and 50 s on the background. Apparent K count rates were enhanced due to the overlap of the Fe 2nd order peak on the PET crystal. Narrowing the detector window enabled us to exclude interfering Fe counts. Setting the PHA (peak height analyzer) to a narrow window width fully excluded 2nd order Fe counts.

Analyses of U and Th in metals were performed by laser ablation inductively coupled plasma mass spectrometry (ICP-MS) at the University of Houston using a Photon Machines Inc. Analyte. 193 ArF laser ablation system coupled to a Varian 810-MS ICP-MS. For all analyses, the laser operated with a repetition rate of 4-10 Hz at 3 J/cm^2, a helium flow rate of 0.5 L/min and a spot size of 50 to 100 μm. Each analysis lasted for a total of 70 seconds, with 20 seconds for background measurements, 30 seconds for ablation, and 20 seconds for washout. We measured chemical concentrations of ^{24}Mg, ^{53}Cr, ^{55}Mn, ^{61}Ni, ^{60}Ni, ^{182}W, ^{185}Re, ^{232}Th and ^{238}U. Analyses were calibrated using NIST 612 and NIST 610 glass standards and corrected for laser and ICPMS elemental fractionation with Ni concentrations measured in metals of run products with EPMA and values of Ni concentrations in standards (Norman et al., 1996; Pearce et al., 1997). Data were reduced using the Glitter software (Achterbergh et al., 1999).

Results

## Textures of experimental run products

All of the samples contain quenched liquid metal and silicate melt (Fig. 1), compositions of which were used for calculating partition coefficients. Orthopyroxene crystals were present in the samples equilibrated at relatively low temperature (Fig. 1D). Three of the U-Th-bearing samples (#904, #907 and #924) also contained U-Th-oxides (with a stoichiometry of UTh_2O_6 or U_2ThO_6) (Fig. 1E-1G). These U-Th-oxides have a euhedral texture and nucleated on other grains, suggesting their crystallization at high temperature due to the saturation of the silicate melt in U and Th, not during the quench. On the other hand, the most reduced samples (PR1577 and PR1578 with log fO_2 of IW-6.5 and IW-6 respectively) contain Si metal crystals embedded in the silicate melts (Fig. 1G). These Si metal crystals have dendritic to skeletal textures, which suggest a formation during the quench. By precaution, in these samples we analyzed the silicate melts in regions free of these crystals. It is likely that these Si metal crystals formed through a reduction reaction of SiO_2 by graphite (originally from the capsule), similar to smelting reactions recently proposed for the surface of Mercury (McCubbin et al., 2017). Most samples contain immiscible Si-rich metal and Fe-rich sulfide ((Morard and Katsura, 2010) (Fig. 1B). However only the samples with high starting sulfur-content have sufficiently large blobs to perform robust analyses. For both U-Th- and K-bearing samples, important quench structures were present within the sulfur-rich phases, with phases of 1 to 10 μm size exsolved from the sulfides (Fig. 1B-C). In order to have chemical compositions of the entire sulfide phase, in each sulfide blob, we performed up to 35 measurements per blob using a defocused beam of 3-30 μm in size and covering approximately the entire surface of the blob (see example in Fig. 1C), and then we averaged these compositions to have compositions of each blob. To retrieve average sulfide chemical composition, we averaged all compositions of the analyzed blobs (see Supplementary Table 1). We initially conducted a test to assess whether there was a difference

11

in the final compositions if we weighted each analysis by the spot size, compared to not weighting. The results show similar compositions within uncertainty. Therefore, for efficiency, we decided to proceed without any weighting. The similarity between weighted and non-weighted data is likely because the variability of the spot size is the same within the whole surface of the sulfide, including homogeneous and heterogeneous regions having quench textures. The consistency of this analytical procedure is also attested by the small variation of chemical compositions of different sulfides blobs within each sample (see Supplementary Table 1).

In three samples (#910, #924 and #921), a temperature gradient within the samples was observed, with a boundary of the capsule containing a larger silicate melt pocket with embedded metal blobs and the remaining part of the sample containing orthopyroxene crystals, silicate melt, liquid metal and sulfide. This texture has been observed in previous multi-anvil experiments (Liebske, 2005). Within the two parts of the samples, each phase was chemically homogeneous (Supplementary Table 1), which attests to local chemical equilibrium. In these samples, chemical compositions were measured in the areas of the sample where metal blobs were the largest, which allowed for a better quantitative trace U, Th or K analysis. Despite the presence of a thermal gradient in the three samples #910, #924 and #921, the calculated partition coefficients were found to be similar within uncertainties with those calculated in the samples free of thermal gradient conducted at the same fO$_2$: log D$_U$ and log D$_{Th}$ from -3.5 to -4.6 in #910, #924, #923 and #907; log D$_K$ of -1.8 in #921 compared to -1.8 to -2.1 in #916 and #919 respectively.

Oxygen fugacity

Oxygen fugacity can be calculated relative to IW buffer based on Fe exchange between metal and silicate:

$$Fe^{metal} + 1/2 O_2 = FeO^{silicate} \tag{1}$$
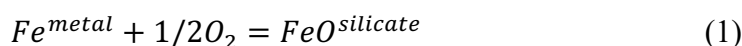
which yields:

$$\Delta IW = \log fO_2{}^{experiment} - \log fO_2{}^{IWbuffer} \tag{2}$$

$$\Delta IW = 2 * \log\left(\frac{x_{FeO}^{silicate} * \gamma_{FeO}^{silicate}}{x_{Fe}^{metal} * \gamma_{Fe}^{metal}}\right) \tag{3}$$

For samples where FeO concentration in the silicate melt is higher than 0.1 mol%, we used an

FeO activity coefficient in the silicate melt $\gamma_{FeO}^{silicate}$ of 1.7 following previous estimates (O'Neill

and Eggins, 2002) and we calculated Fe activity coefficient in the metal γ_{Fe}^{metal} using the online

metal activity calculator (Wade et al., 2012).

For samples having less than 0.1 mol% FeO in the silicate melts, we calculated fO$_2$

utilizing the equilibrium (following (Cartier et al., 2014; Namur et al., 2016a)):

$$Si^{metal} + O_2 = SiO_2{}^{silicate} \tag{4}$$
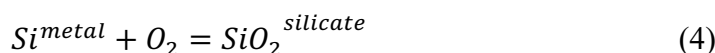
The equilibrium constant of this reaction can be expressed as a function of temperature T, gas

constant R, and Gibbs free energy ΔG^0 or as a function of T, R, pressure P, enthalpy change

ΔH_r^0, entropy change ΔS_r^0, and volume change ΔV of the reaction:

$$\ln K_{eq}(4) = \ln \frac{a_{Si}^{metal} * fO_2}{a_{SiO_2}^{silicate}} = -\frac{\Delta G^0}{RT} = -\frac{(\Delta H_r^0 - T\Delta S_r^0 + \int \Delta V dP)}{RT} \tag{5}$$

ΔH_r^0, ΔS_r^0 and ΔV were calculated using thermodynamic tables from (Robie and Hemingway,

1995). We considered $a_{SiO_2}^{silicate} = 1$, $a_{Si}^{metal} = x_{Si}^{metal} * \gamma_{Si}^{metal}$, with the latter also calculated

(as for γ_{Fe}^{metal}) using the online activity calculator. The fO$_2$ was then calculated relative to IW

buffer using Eq. (2) and the relationship between pressure (P), temperature (T) and the fO$_2$ of

IW buffer, given by (Huebner, 1971):

13

$$\log fO_2{}^{IWbuffer} = 6.471 - \frac{26834}{T} + 0.055 * \frac{P-1}{T} \tag{6}$$

Our samples have an fO_2 ranging from ΔIW-6.5 to ΔIW-2.3. Errors on fO_2 were

previously estimated to be lower than 0.5 log units (Namur et al., 2016a).

U, Th and K partitioning

Our results show lower partition coefficients for U and Th between metal and silicate

(log $D^{met/sil}$ of -5 to -2 for U and -6 to -3 for Th) compared to those between sulfide and silicate

(log $D^{sulf/sil}$ of ~0.3 for U and ~ -0.8 for Th) (Fig. 2). This difference in partitioning is less

pronounced for K (log $D^{met/sil}$ of -3.9 to -1.7 and log $D^{sulf/sil}$ of -2.6 to -1.5) (Table 2). For K and

U, several studies have previously reported partition coefficients at high pressure and

temperature (Blanchard et al., 2017; Bouhifd et al., 2013; Bouhifd et al., 2007; Chidester et al.,

2017; Corgne et al., 2007; Mills et al., 2007; Steenstra et al., 2018; Wohlers and Wood, 2015;

Wohlers and Wood, 2017). For Th, there are a few studies that previously measured its

partitioning (Wohlers and Wood, 2015; Wohlers and Wood, 2017). Our data are

complementary to these previous studies as they expand the database to conditions where metal

and sulfide are both present. In studies of (Wohlers and Wood, 2015; Wohlers and Wood,

2017), oxygen fugacity and chemical compositions of coexisting metals were not provided. We

therefore calculated the ΔIW of their samples using Eq. 3, and estimates of a_{Fe}^{metal} in their

virtually coexisting metals. We considered $a_{Fe}^{metal} = 1$ for the most oxidized samples where

silicate melt has a $x_{FeO}^{silicate}$ higher than 0.02. The Fe metal activities for more reduced samples

were derived from a linear relationship between activity of Fe metal (a_{Fe}^{metal}) in S-poor metals

and FeO molar fraction in silicate melt ($x_{FeO}^{silicate}$) based on our data and those of previous

studies ($a_{Fe}^{metal} \sim 34.9797 * x_{FeO}^{silicate} + 0.3026$). This calculation of the fO_2 was not used in any

of the following models, but only to be able to plot and compare all partition coefficients for

metals and sulfides (Fig. 2).

14

We considered two different equilibria for analyzing metal-silicate and sulfide-silicate partition coefficients. $D^{met/sil}$ of element M can be described by the following reaction:

$$MOn_{/2}{}^{silicate} = \frac{n}{4}O_2 + M^{metal} \qquad (7)$$
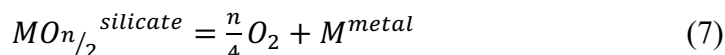
The equilibrium constant of reaction (7) is expressed as a function of fO_2 (or O_2 activity):

$$-\Delta G°(7)/RT = \ln\left(\frac{fo_2{}^{n/4} * a_{M^{met}}}{a_{MOn_{/2}}{}^{silicate}}\right) = \ln\left(\frac{fo_2{}^{n/4} * x_{M^{met}} * \gamma_{M^{met}}}{x_{MOn_{/2}}{}^{silicate} * \gamma_{MOn_{/2}}{}^{silicate}}\right) \qquad (8)$$

Where $\Delta G°(7)$ is the free energy of the reaction (7), n is the valence of element M in the silicate, and a, x and γ are the activities, molar fractions and activity coefficients of the chemical species respectively. Re-arranging, the partition coefficient of the element M can be expressed as:

$$\log D_M^{met/sil} = \log \frac{x_{M^{metal}}}{x_{MOn_{/2}}{}^{silicate}} = -\Delta G°(7)/(2.303 * RT) - \frac{n}{4} * \log fO_2 - \log \frac{\gamma_{M^{metal}}}{\gamma_{MOn_{/2}}{}^{silicate}}$$

(9)

$D^{sulf/sil}$ of element M can be described by the equilibrium:

$$MO_{n/2}^{silicate} + \left(\frac{n}{2}\right)FeS^{sulfide} = MS_{n/2}^{sulfide} + \left(\frac{n}{2}\right)FeO^{silicate} \qquad (10)$$
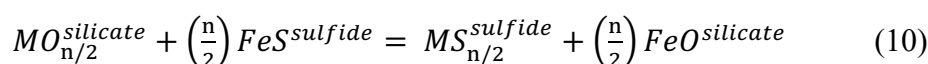
The equilibrium constant of this reaction is expressed as:

$$\ln K(10) = \ln\left(\frac{a_{MS_{n/2}}^{sulfide} * a_{FeO}^{silicate^{n/2}}}{a_{MO_{n/2}}^{silicate} * a_{FeS}^{sulfide^{n/2}}}\right) = \ln\left(\frac{x_{MS_{n/2}}^{sulfide} * \gamma_{MS_{n/2}}^{sulfide}}{x_{MO_{n/2}}^{silicate} * \gamma_{MO_{n/2}}^{silicate}}\right) + \frac{n}{2}\ln\left(\frac{x_{FeO}^{silicate} * \gamma_{FeO}^{silicate}}{x_{FeS}^{sulfide} * \gamma_{FeS}^{sulfide}}\right) =$$

$$-\frac{\Delta G^0(10)}{RT} \quad (11)$$

Therefore, partition coefficient of element M between sulfide and silicate can be expressed as:

$$\log D_M^{sulf/sil} = \log \frac{x_{MS_{n/2}}^{sulfide}}{x_{MO_{n/2}}^{silicate}} = -\frac{\Delta G°(10)}{2.303*RT} - \log\left(\frac{\gamma_{MS_{n/2}}^{sulfide}}{\gamma_{MO_{n/2}}^{silicate}}\right) + \frac{n}{2} * \log\left(\frac{x_{FeS}^{sulfide} * \gamma_{FeS}^{sulfide}}{x_{FeO}^{silicate} * \gamma_{FeO}^{silicate}}\right) \quad (12)$$

15

Discussion

In the following discussion, we use our experimental data to derive expressions predicting HPE partitioning between metal, silicate and Fe sulfide. These equations are then utilized to calculate the distribution of HPE between the core, mantle and possible sulfide layer of Mercury and assess their bulk planetary concentrations. From this core formation model, we also discuss the implications for Mercury's volatile content and fractionation of K/U and K/Th ratios.

Prediction of partition coefficients for U, Th, and K

Activities of elements in metals or sulfides are known to be dependent on the chemical composition of light elements in the metal or sulfides, such as Si, S, C and O. We modeled this dependency using simplified expressions based on the epsilon formalism for multicomponent metallic systems (Ma, 2001). The effect of silicate melt composition on activity coefficients in silicate melts is commonly approximated by a factor proportional to the structural parameter nbo/t (ratio of non-bridging oxygens to tetrahedrally coordinated cations). To account for these effects of chemical composition, Eq. (9 & 12) become:

$$\log D_M^{met/sil} = \frac{X_{met}^M}{X_{silicate}^M} = a + \frac{b}{T} + c * \frac{P}{T} + d * \log f_{O_2} + e * \frac{T_0 * \log\left(1 - X_S^{met}\right)}{T} + f *$$

$$\frac{T_0 * \log\left(1 - X_C^{met}\right)}{T} + g * \frac{T_0 * \log\left(1 - X_{Si}^{met}\right)}{T} + h * \frac{T_0 * \log\left(1 - X_O^{met}\right)}{T} + i * nbo/t \qquad (13)$$

$$\log D_M^{sulf/sil} = \log \frac{X_{sulf}^M}{X_{sil}^M} = a + \frac{b}{T} + c * \frac{P}{T} + d * \log X_{FeO}^{sil} + e * \frac{T_0 * \log\left(1 - X_S^{sulf}\right)}{T} + f *$$

$$\frac{T_0 * \log\left(1 - X_C^{sulf}\right)}{T} + h * \frac{T_0 * \log\left(1 - X_O^{sulf}\right)}{T} + i * nbo/t + j * \frac{T_0 * \log\left(1 - X_S^{sil}\right)}{T} \qquad (14)$$

Where X_{met}^M, $X_{silicate}^M$ and X_{sulf}^M are the mass concentrations (in wt%) of element M in the metal, silicate and sulfide liquids respectively and T_0 is a reference temperature of 1873 K. The parameter d in Eq. (13) and Eq. (14) corresponds to –n/4 and –n/2 respectively (with n the

16

valence of U, Th and K in silicate melt), and $\log f_{O_2}$ is relative to IW buffer. We considered a valence state of 2+ for U in silicate melts, as recently suggested by (Blanchard et al., 2017; Chidester et al., 2017). Because U and Th have very close chemical properties, Th is also expected to have a valence of 2+ in silicate melts. We assumed that K is present as K^+ in silicate melts, which is corroborated by the observed weaker correlation between $\log D^{met/sil}$ and ΔIW for K than for U and Th (see below and Fig. 4B).

We considered the effect of S concentration in the silicate melt (X_S^{sil}), as it was previously shown that it interacts with FeO in the silicate melt and affects its activity coefficient (Righter, 2003; Wohlers and Wood, 2017). Constants a, b, c, e, f, g, h, i and j were determined with a linear regression fit (results given in Table 3). In our experimental charges and in several other reported studies, U, Th and K were doped at higher levels than in natural materials (concentrations corresponding to several wt% in comparison to ppm and ppb levels). Highly doped samples may lead to deviation from Henry's law. However, previous studies showed that Henry's law violation does not affect partitioning behavior of these elements (Chidester et al. 2017, Corgne et al. 2007). These findings are supported by the good predictions of experimental partition coefficients using our regressions, for example for samples containing concentrations of U in silicates from 117 ppm (Wohlers & Wood, 2015) to 66 wt% (Chidester et al. 2017). For all three elements, we fitted Eq. 13-14 using our experimental data and by selecting previous data where O was measured in metals and sulfides (Blanchard et al., 2017; Bouhifd et al., 2013; Bouhifd et al., 2007; Chidester et al., 2017; Corgne et al., 2007; Mills et al., 2007; Steenstra et al., 2018; Wohlers and Wood, 2015; Wohlers and Wood, 2017).

We performed usual p-value tests and selected results for constants a to j when these are statistically significant (Table 3). The quality of the fits is shown through standard deviation 1σ, correlation coefficients, F and p-values given in Table 3 and through the comparison between measured and calculated partition coefficients (Fig. 3). We found a similar result for a

17

positive effect of temperature on $D^{met/sil}$ to recent studies conducted at very high pressure and temperature using diamond anvil cells: b= -10300 compared to -11000 and -10133 in (Blanchard et al., 2017; Chidester et al., 2017). Pressure effects were not resolvable for any partition coefficient. A positive effect of O in sulfide on $D^{sulf/sil}$ for K, U and Th and positive effect of S-content in silicate on $D^{sulf/sil}$ for U and Th are also in agreement with previous findings (Blanchard et al., 2017; Corgne et al., 2007; Wohlers and Wood, 2017) (Fig. 4A). Altogether, we found that:

- U, Th, and K become more siderophile or chalcophile with decreasing fO_2 or FeO content in the silicate respectively (Fig. 2 & 4). The lower valence state of K than U and Th induces a weaker effect of fO_2 and FeO content on K than U and Th partitioning.

- U, Th and K partition more efficiently into sulfides than into metals. This difference of affinity is however, stronger for U and Th than for K (Fig. 2).

- Increasing oxygen content in sulfides enhances $D^{sulf/sil}$ of U, Th and K (Fig. 4A). Increasing S content of the silicate melt induces an increase of $D^{sulf/sil}$ for U and Th and a decrease for K (Fig. 4A).

- Silicon in metal decreases K partitioning between metal and silicate (Fig. 4B). Oxygen in metal increases and decreases $D^{met/sil}$ of U and Th respectively (Fig. 4B). The effect of O on U partitioning into metals is however, better constrained than for Th. Additional data at more oxidized conditions would be useful to precisely address this effect.

It is also important to note that available experimental data on U, Th and K partition coefficients between sulfide and silicate from our study and the literature are conducted at a log fO_2 equivalent or higher than IW-4.2, yielding in the silicate melt a minimum concentration of 0.35 wt% FeO and a maximum S concentration of 11 wt%. For the entire range of available experimental conditions, the highest measured values of log $D^{sulf/sil}$ are 1.2 for U, -0.14 for

Th and -0.6 for K. Here, in the model of Mercury's differentiation presented below, we extrapolated our thermodynamic models (Eq. 13-14) for sulfide-silicate partitioning to a minimum fO_2 of 5.5 log units below the IW buffer, yielding a maximum log $D^{sulf/sil}$ of 1.35 for U, 0.6 for Th and 0.07 for K (see Table 3). Extrapolations to extremely reducing conditions yield much higher partition coefficients: log $D^{sulf/sil}$ for U and Th would be of ~3 and ~6 at log fO_2= IW-6 and IW-7.3 respectively. In future studies, it would be interesting to perform additional experiments at very low fO_2 and S-saturated samples, to investigate how U, Th and K partition into sulfides at these extremely reducing conditions. A consequence of all these effects on the partitioning of U, Th and K is that the three elements will likely distribute differently between core, mantle and possible sulfide layer, which is expected to fractionate K/U and K/Th ratios during Mercury's core formation.

Fe-Si-S-C-O composition of Mercury's core and possible sulfide layer

Partitioning of U, Th and K depends on the chemical compositions of metals and sulfides. Therefore, application of our results requires knowledge of the Fe-Si-S-C-O contents of sulfide and metallic liquids relevant to Mercury's core formation. As a result, we derived new expressions that quantify Si and O partitioning between metal (or sulfide for O) and silicate, and that estimate S-content and C-content in sulfides and metals.

Silicon partitioning between metal and silicate.

We considered previous and present (this study) experimental data on equilibria at very low fO_2 down to IW-8 (Bouhifd and Jephcoat, 2011; Boujibar et al., 2014; Cartier et al., 2014; Chabot et al., 2014; Chidester et al., 2017; Fischer et al., 1994; Ricolleau et al., 2011; Siebert et al., 2012; Suer et al., 2017; Tsuno et al., 2013; Tuff et al., 2011) and by taking into account of interactions between Si, S, C and O in the metals. Silicon exchange between metal and silicate can be described by the following reaction:

19

$$SiO_2{}^{silicate} = Si^{metal} + O_2 \qquad (15)$$
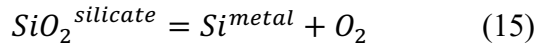
Eq. (13) can be used to determine Si partitioning between metal and silicate, considering a valence of 4+ for Si in silicate melt and without using the term $g * \frac{\log(1-X_{Si})}{T}$. For the lowest values of fO_2 (< IW-4.5), a first regression yielded unrealistic concentrations of Si in metal (>100 wt%). This could indicate a change of Si valence state in silicate melts to a mixture of Si^{4+} and Si^{2+} (as for U) or a drastic change of Si activity coefficient in metal at very low fO_2. Therefore, for the very low fO_2 conditions (< IW-4.5), we added the term $j * (\log(f_{O_2}))^2$ to the regression, in order to be able to predict Si partitioning. In these fO_2 conditions, Si partition coefficient is modelled with the expression:

$$\log D_{Si}^{met/sil} = \frac{X_{metal}^{Si}}{X_{silicate}^{SiO_2}} = a + \frac{b}{T} + c * \frac{P}{T} + d * \log f_{O_2} + e * \frac{T_0 * \log(1-X_S)}{T} + f *$$

$$\frac{T_0 * \log(1-X_C)}{T} + h * \frac{T_0 * \log(1-X_O)}{T} + i * nbo/t + k * (\log(f_{O_2}))^2 \qquad (16)$$

where X_{metal}^{Si} and $X_{silicate}^{SiO_2}$ are the concentrations of Si in the metal and SiO_2 in the silicate respectively (in wt%). A regression fit was conducted first for data at log fO_2 >IW-4.5 to retrieve constants a to i, then for the more reduced data, by fixing the latter constants and investigating intercept a and parameter k (Fig. 5). We found that Si becomes more siderophile with decreasing fO_2 (Table 3) and increasing temperature and O content of the metal, in agreement with previous studies (Fischer et al., 2015; Siebert et al., 2012; Tsuno et al., 2013), while S and C effects are found statistically insignificant (Table 3).

Sulfur and carbon in the Fe-rich core.

To address sulfur and carbon concentrations in the Fe-rich core (X_S^{metal} and X_C^{metal} respectively), we derived expressions as a function of Si content in the core. We used data from (Cartier et al., 2014) that span the range of fO_2 typical of Mercury's core segregation (down to IW-8) and were conducted at 5 GPa, which is the approximate pressure at Mercury's core-

20

mantle boundary and thus the conditions of differentiation. We found that X_S^{metal} and X_C^{metal} are negatively correlated with X_{Si}^{metal} (Fig. 6B-C), following the expressions:

$$X_S^{metal} = 2.6485 * \exp\left(-0.097 * X_{Si}^{metal}\right) \tag{17}$$

$$X_C^{metal} = -0.2886 * X_{Si}^{metal} + 6.4038 \tag{18}$$

Carbon in the metal remains low at high Si content (X_C^{metal} <1.5 wt% when X_{Si}^{metal} >16 wt%) and becomes close to 0 when Si >22.2 wt% (Fig. 6B). Eq (18) is therefore only used for conditions where X_{Si}^{metal} is lower than 22.2 wt%.

Oxygen in metal and sulfide.

O partitioning between metal and silicate can be described by the equilibrium:

$$FeO_{silicate} = Fe_{metal\ or\ sulfide} + O_{metal\ or\ sulfide} \tag{19}$$
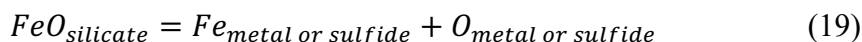
for which the equilibrium constant can be expressed as a function of its Gibbs free energy ($\Delta G°$) following:

$$\log K(3) = \Delta G°(3)/(2.303RT) = \log a_{Fe}^{met/sulf} - \log a_{FeO}^{sil} + \log a_O^{met/sulf} \tag{20}$$

where $a_{Fe}^{met/sulf}$, $a_O^{met/sulf}$ and a_{FeO}^{sil} are activity coefficients of Fe and O in the metal or sulfide and FeO in the silicate, respectively. Re-arranging and combining with previous Fe-O equilibria (Eq. 3) yields:

$$\log X_O^{met/sulf} = \Delta G°(20)/(2.303RT) + \Delta IW/2 - \log \gamma_O^{met} \tag{21}$$

Where $X_O^{met/sulph}$ is the concentration of O in the metal or sulfide. In a similar way as for U, Th, K and Si, when taking into account of pressure, temperature and chemical compositions, $X_O^{met/sulph}$ can be expressed as:

21

$$\log X_O^{met \; or \; sulf} = a + \frac{b}{T} + c*\frac{P}{T} + d*\log f_{O_2} + e\frac{T_0*\log(1-X_S)}{T} + f*\frac{T_0*\log(1-X_C)}{T} + g*$$

$$\frac{T_0*\log(1-X_{Si})}{T} \tag{22}$$

X_S, X_C, and X_{Si} are weight fractions of S, C and Si in the metal or sulfide respectively. We used previous data from similar studies to those used for Si, U, Th and K partitioning and additional data from (Asahara et al., 2004; Corgne et al., 2008; Rubie et al., 2004) to derive parameters a to g using a linear regression. Fitted parameters are given in Table 3, and are in agreement with previous studies showing a positive effect of pressure, temperature and Si-content in metals on the siderophile character of O (Bouhifd and Jephcoat, 2011; Fischer et al., 2015; Rubie et al., 2004; Siebert et al., 2012; Tsuno et al., 2013). We additionally found positive effects of S and C on O partitioning (Table 3). Comparison between measured and calculated O content in metal and sulfide is shown in Fig. 5A.

Resulting compositions of Mercury's core and sulfide layer.

During planetary accretion, internal pressures and temperatures of equilibration between core and mantle increase progressively. Modeling this continuous accretion process can only be conducted by making assumptions on bulk concentrations of the elements in accreted bodies. Here, the principal aim of the study is to investigate bulk planetary HPE ratios. Therefore, instead, we modeled core formation as a single stage process, using concentrations in crusts and mantles, in order to avoid making assumptions on initial HPE in building blocks. We assumed that Mercury's core and mantle fully equilibrated (a reasonable assumption based on findings on the thermal evolution of Mercury in (Tosi et al., 2013)) in a single stage core formation model at a pressure and temperature corresponding to those of core-mantle boundary (5.5 GPa) and corresponding Mercurian mantle liquidus temperature (2230 K (Namur et al., 2016b)). Concerning nbo/t, we assumed a value of 1.45 based on modeled mantle composition of Mercury (Nittler et al., 2018). We explored several fO$_2$ scenarios where it is comprised within

22

the range proposed in previous studies (IW-7.3 to IW-2.6) (McCubbin et al., 2012; McCubbin et al., 2017; Namur et al., 2016a; Zolotov et al., 2013). For models including a sulfide layer, we considered fO_2 between IW-4 and IW-5.5, which is the average fO_2 of Mercury's surface based on S concentration on the surface (Namur et al., 2016a). Indeed, extrapolated partitioning of U and Th using our thermodynamic models become very high at log $fO_2 \leq$ IW-6 (log $D^{sulf/sil} > 3$ for U and Th), and immiscibility is not expected to occur at log $fO_2 \geq$ IW-3 (Morard and Katsura, 2010).

To estimate Mercury's Fe-rich core composition, for each considered fO_2, we first calculated Si concentration of the core using Eq. (16) and a SiO_2 concentration of bulk silicate Mercury of 52.8 wt% (Nittler et al., 2018) (Fig. 6A). We found an abundance of Si in the core ranging from 0.8 to 66 wt% for models where fO_2 is from IW-2.6 to IW-7.3 (Table 4). We then used our derived relationships between concentrations of Si, S and C (Eq. (17-18)) to calculate S and C abundances in the core (Fig. 6B-C). Maximum concentrations of S and C in the core are 6.2 and 2.5 wt% respectively for the most oxidized conditions (IW-2.6). Their abundances approach zero for a core equilibration at IW-5. Oxygen concentration in the metal was also calculated using our regression (see above, Eq. 22) and was found equal to 0 for all considered fO_2. Fe and Ni concentrations in the core were estimated using the difference of all considered light elements to 100% and assuming a chondritic Fe/Ni mass ratio of 17.5 (Wasson and Kallemeyn, 1988). This is a reasonable assumption since Ni is very siderophile in reduced conditions and thus segregated significantly into Mecury's core. Resulting core compositions are given in Table 4.

The analysis of the ternary diagram at 6 GPa (Morard and Katsura, 2010) combined with calculated core compositions for each considered fO_2 suggests that if Mercury's core equilibrated at an fO_2 of IW-3 or higher, it would be unlikely to have formed an immiscible S-poor metal and sulfide layer. Therefore, for the two scenarios where fO_2 is IW-3 and IW-2.6,

23

we did not consider any sulfide layer. For the Fe sulfide, there is no systematic study on C

solubility in sulfides as a function of fO$_2$. We hence assumed a concentration of 1 wt% C,

which is within the range measured in our samples (0-2 wt% Supplementary Table 1). O

concentration in sulfide was calculated using Eq. (22) and found very low (0.02 to 0.09 wt%).

Fe, S and Ni concentrations were then calculated by mass balance and stoichiometry,

considering a chondritic Fe/Ni ratio (17.5) (Table 4).

Model of U, Th and K partitioning during core formation

U, Th and K distribution between mantle, core and sulfide was calculated using Eq. (13-

14) (Table 4), calculated core and sulfide layer compositions, and FeO and S concentrations of

bulk silicate Mercury (Table 4). FeO was calculated for each considered fO$_2$ using the

corresponding core composition, and using the same methods for estimating Fe activity

coefficients as for our fO$_2$ calculations for our samples (see Eq. (3) above). To calculate

abundances of HPE in the possible sulfide layer, it was also necessary to make an assumption

on the S abundance of the S-saturated magma ocean or bulk silicate Mercury. This sulfur

content was calculated based on a previously published expression giving S solubility in silicate

melts (Namur et al., 2016a) (Table 4). Only models considering the presence of a sulfide layer

are affected by S content in silicate, as $D_{met/sil}$ is not dependent on this parameter.

For a sulfide layer-free Mercury, bulk Mercury concentrations of U, Th and K (X_M^{bulk})

were calculated by mass balance and using concentrations of bulk silicate Mercury (X_M^{BSM}, see

below) together with Eq. (13) giving partition coefficients $D_M^{met/sil}$:

$$X_M^{bulk} = (1 - f_{core}) * X_M^{BSM} + f_{core} * X_M^{BSM} * D_M^{met/sil} \qquad (23)$$

where f_{BSM} and f_{core} are the mass fractions of BSM and cores respectively. We used a Fe-rich

core mass fraction of 0.68 as suggested by its gravity field (Hauck et al., 2013). For models

24

including a sulfide layer, we varied the layer mass fraction from 0 to 0.15 and derived $D_M^{sulf/sil}$

from Eq. (14). Similarly, bulk elemental concentrations are calculated by mass balance using:

$$X_M^{bulk} = (1 - f_{core} - f_{sulfide}) * X_M^{BSM} + f_{core} * X_M^{BSM} * D_M^{met/sil} + f_{sulfide} * X_M^{BSM} *$$

$$D_M^{sulf/sil} \qquad (24)$$

We calculated the thickness of the FeS layer considering a density of Mercury's mantle

of 3000 kg.m^{-3} (an intermediate value within the range given in (Hauck et al., 2013): 2800-

3600), and a sulfide density of 4400 kg.m^{-3} (Nishida et al., 2008). A previous experimental

study showed that the density of metal alloys depends on their Si content: 6.75 and 5.6 g.cm^{-3}

for 20 and 50 wt% Si respectively (Tateyama et al., 2011). These experimental results are

therefore used to estimate liquid and solid core densities, which are assumed to be similar since

Si partitioning between solid and liquid alloys is close to unity (Morard et al. 2014, Fischer et

al. 2013, Knibbe & van Westrenen 2015). Depending on the fO$_2$ (IW-4, IW-5 and IW-5.5) and

hence core composition, we found that sulfide layer mass fractions of 1, 5, 10 and 15 wt%

correspond to thicknesses of 14±1, 67±4, 131±8 and 191±11 km respectively during core-

mantle differentiation. This range of the possible sulfide layer thickness is consistent with

previous estimates based on the moment of inertia of Mercury (Hauck et al., 2013; Smith et al.,

2012). The relative fractions of solid and liquid core and the state of the sulfide layer are actually

poorly constrained. If the sulfide layer solidified to the present time and with a significant

compaction of Mercury's interior, given values of thicknesses are likely to be overestimated.

Implications for bulk planet Fe, Si and S concentrations

Based on previously published Mercury's mantle composition (Nittler et al. 2018) and

our calculated core compositions given in Table 3, we compared resulted bulk Mercury S (Fig.

7A) and Fe/Si (Fig. 7B) with those of main chondrites (enstatite, ordinary and carbonaceous

chondrites) (Nittler et al. 2004). For Fe/Si ratio, the lower the fO$_2$, the higher the Si

concentration is in the core and therefore the lower bulk Mercury Fe/Si ratio (Fig. 7B). In addition, increasing the thickness of the sulfide layer yields higher Fe/Si. Bulk sulfur is also negatively correlated with fO_2 in the range of IW-7.3 to IW-4 and positively correlated with the thickness of the sulfide layer (Fig. 7A). For any given bulk planetary S content, lower fO_2 of core/mantle differentiation would yield higher S in bulk silicate Mercury (BSM) (from 1.7 to 23 wt% when fO_2 decreases from IW-2.6 to IW-7.3), due to its increasing chalcophile character with reducing conditions (e.g. Boujibar et al. 2014, Namur et al. 2016a). As a result, lower fO_2 yields a thinner sulfide layer, as more S is dissolved in BSM and less S is available to saturate and form sulfides (Fig. 7A). Conversely, the greater the bulk S content of Mercury's building blocks, the larger the thickness of the sulfide layer would be. However, it is important to point out that at relatively oxidized conditions (IW-3 and IW-2.6), S concentration in the core is very close to that of BSM (1.7-2.5 wt% S, see Table 4). Therefore, in these oxidized conditions, where a sulfide layer is not expected to exist, bulk sulfur content is controlled by its partitioning between BSM and the Fe-rich core, whereas in reduced conditions it is controlled by S solubility in BSM. Therefore, due to the large core of Mercury, without any sulfide layer, oxidized conditions (IW-3 and IW-2.6) yield a similar or higher bulk S content than at IW-4 and IW-5 (see Fig. 7A).

Overall, our results show that the considered ranges of core composition and sulfide layer thickness can yield a bulk S concentration and Fe/Si similar to those found in chondrites (Nittler et al. 2004). Models where the fO_2 is relatively high (IW-3 to IW-2.6) and those with a fO_2 of IW-4 and a thick sulfide layer (>130 km) however yield a higher Fe/Si ratio than chondritic values. Current internal structure models of Mercury consider a maximum Si concentration in the core of 25 wt% (e.g. Knibbe & van Westrenen 2015). It is necessary in future studies to investigate if our estimations of core composition yield a moment of inertia consistent with MESSENGER measurements.

26

Implications for volatile content in Mercury

Our model allows calculating K, U and Th concentrations in Mercury's core and possible sulfide layer. With the absence of a sulfide layer, bulk K/U and K/Th stay basically similar to the surficial values, even with an fO_2 as low as IW-7.3: for the whole range of fO_2 (IW-7.3 to IW-2.6) bulk K/U = 12550 ±450 and K/Th = 5240 ±20 in comparison to surface K/U = 12800 ±4300 and K/Th = 5200 ±1800. If an sulfide layer actually exists, both K/U and K/Th of bulk Mercury would be lower than those measured on the surface in some specific fO_2 conditions (Fig. 8). At IW-4, the K/Th ratio becomes slightly higher than surficial values with increasing the thickness of the sulfide layer. This effect results from a lower abundance of Th than K in the sulfide relative to the mantle, which is due to the opposite effect of the abundance of S in the silicate on $D^{sulf/sil}$ of K and Th or U (Fig. 4A). On the other hand, in order to decrease K/U and K/Th ratios, reducing conditions (<IW-4) would be required. With a core-mantle equilibration occurring at a fO_2 close to IW-5.5, a sulfide layer of at least 190 km thickness allows reducing K/U ratio to a lower value than those of the other terrestrial planets (Fig. 8A). In the same conditions, bulk Mercury K/Th becomes close to Venus' and Earth's ratios (Fig. 9). For this scenario, bulk S content of Mercury is close to the maximum chondritic values (6-7 wt% in some carbonaceous chondrites (Nittler et al., 2004)), suggesting an accretion of material rich in sulfur (Fig. 7).

Our thermodynamic models show that all three heat-producing elements U, Th and K become more chalcophile with decreasing the oxygen fugacity or the FeO content of the silicate melt (Table 3 & Fig. 2). However, this effect is more pronounced for U and Th than for K. It is therefore expected that both K/U and K/Th fall within an overall volatile depletion trend described by the terrestrial planets if Mercury contains an iron sulfide layer formed at very low fO_2 (possibly IW-6 and lower). Additional experiments at an oxygen fugacity lower

27

than IW-5.5 would be important to confirm this effect. Our results still show that Mercury's

surface K/U and K/Th should not exclusively be interpreted as a volatile enrichment, but can

also point to a sequestration of more U and Th than K in a sulfide layer, if it exists.

MESSENGER spacecraft measured relatively high concentrations of other volatile elements

such as S, Na and C and a chondritic Cl/K ratio (e.g. Nittler et al., 2018), which should also be

modeled in the context of core formation to fully address Mercury's volatile depletion.

Moreover, if the magma ocean becomes saturated in sulfur before it fully crystallizes, sulfide

phases could potentially sink and accumulate at the base of the mantle. However, it is still

unclear if the chemical composition of such sulfides would deviate from FeS endmember and

become enriched in Ca and Mg. It would be interesting in future studies to address the effect

of Mg and Ca present in sulfides on the partitioning of these heat producing elements.

Implications for radioactive heat generation

Internal heat generated by the decay of radiogenic isotopes ^{238}U, ^{325}U, ^{232}Th and ^{40}K

present in the mantle, crust and metallic core of Mercury at the present day time was

calculated, using natural abundances of the isotopes (N_0), their half-lives (λ) and heat

produced per mass of isotopes given in Lodders (2003) and Turcotte & Schubert (2002). The

mass fraction N of each isotope at any time t is expressed as:

$$N = N_0 * e^{-\lambda t} \tag{25}$$

We considered that HPE concentrations in Mercury's crust are similar to those measured

on the surface by MESSENGER gamma ray spectrometer (Peplowski et al. 2011), and that

mantle concentrations are equivalent to 0 to 20 % those measured on the surface. These values

are consistent with ranges of U, Th and K partitioning between major mantle phases and silicate

melts $D_{mant/crust} \ll 1$ to $D_{mant/crust} = 0.2$ given in the literature (Blundy and Wood, 2003). Mercury's

crust is assumed to represent 10 wt% bulk silicate Mercury, corresponding to a crustal thickness of 30 km, an intermediate value between ranges constrained by geophysical studies (Padovan et al. 2015, Sori 2018). It is worth noting that assumptions on HPE concentrations in the mantle relative to the crust does not affect results on bulk planetary K/U and K/Th, because U, Th and K behave in a similar way during global silicate magmatic differentiation. This parameter is only important when calculating heat flow, which depends on absolute concentrations in Mercury's layers.

Results show that the assumption of the concentrations of HPE in Mercury's mantle is the major controlling parameter for total heat production. Since concentrations of HPE in Mercury's Si-rich core are low, with the absence of a sulfide layer, bulk radioactive heat generation is almost exclusively limited to that produced by the mantle and crust. Therefore, in the case of absent sulfide layer, varying the fO_2 of Mercury's differentiation affects weakly the total heat generated, which is found of 0.38 and 2.1 TW at the present time and at 4.5 Ga. On the other hand, the potential presence of a sulfide layer decreases heat production by up to one third if it is as thick as 190 km and with moderate fO_2 (IW-4 and IW-5) (Fig. 10). This result is a consequence of lower total concentration of U, Th and K in sulfides than in silicates at IW-4 to IW-5. For models where the fO_2 is as low as IW-5.5, the presence of sulfides does not affect significantly heat production (Fig. 10). It is important to note that partition coefficients of these heat-producing elements between sulfide and silicate become higher with decreasing fO_2, so it is possible that the iron sulfide layer contains more U, Th and K and generated more radioactive heat than the bulk silicate mantle, if it formed in an extremely reduced environment. Additional experimental data to precisely determine their behavior at extremely low fO_2 (<IW-5.5) would be useful to investigate whether the presence of a FeS layer can increase total heat budget in Mercury.

29

Conclusions

Our experimental data show that U, Th and K partition more efficiently into sulfides than into metals. U and Th partitioning is stronger than for K at low fO_2. Hence, bulk K/U and K/Th ratios of planetary bodies, especially those containing a sulfide layer can be fractionated. This partitioning is more pronounced at low fO_2 and is affected by other compositional parameters. O content in the sulfide increases $D^{sulf/sil}$, while S content in the silicate increases $D^{sulf/sil}$ for U and Th and decreases it for K. For metal-silicate equilibria, $D_U^{met/sil}$ increases with temperature and O content in the metal, while $D_{Th}^{met/sil}$ and $D_K^{met/sil}$ decrease with O and Si contents of the metal respectively.

Using our data and those from the literature, we provided chemical compositions of the Fe-rich core and possible sulfide layer for the range of fO_2 proposed for Mercury's differentiation (IW-7.3 to IW-2.6). We used these chemical compositions and partitioning of U, Th and K to model their fractionation during Mercury's core formation. We show that without any sulfide layer between core and mantle, K/U and K/Th ratios remain close to the surface values. If an FeS layer exists and Mercury's core differentiated at IW-5 or more oxidized conditions, both ratios would still remain higher than Venus'. K/U and K/Th ratios decrease to values close to or lower than Venus if the fO_2 of core formation is close to IW-5.5 or lower and with the presence of a sulfide layer at least 130 km thick. In such conditions, Mercury's bulk K content could be as low as Earth and Venus and lower than Mars, resulting from a volatile depletion in the inner part of the Solar System. However, other processes should address elevated Na, C and S concentrations and chondritic Cl/K ratios measured on the surface.

For the partitioning between sulfide and silicate, since our experimental data and those of previous studies are limited to fO_2 higher than IW-4.2, the extrapolations to lower fO_2 than IW-5.5 yield extensively high partition coefficients of U and Th. Therefore, it is essential in

30

future studies to experimentally determine this partitioning in very reducing conditions, as the fractionation of HPE within Mercury's reservoirs would be even greater. However, for such models of a very reduced Mercury (especially lower than IW-7), containing a sulfide layer, as S in bulk silicate Mercury would be very high, bulk Mercury S content could be super-chondritic.

Acknowledgments

References

Achterbergh, v., Ryanm, E., and Griffin, W.L. (1999) GLITTER: On-line interactive data reduction for the laser ablation ICP-MS microprobe. Proceedings of the 9th V. M. Goldschmidt Conference, p. 305-306, Cambridge, Massachusetts.

Albarède, F. (2009) Volatile accretion history of the terrestrial planets and dynamic implications. Nature, 461, 1227-1233.

Asahara, Y., Kubo, T., and Kondo, T. (2004) Phase relations of a carbonaceous chondrite at lower mantle conditions. Physics of The Earth and Planetary Interiors, 143–144(0), 421-432.

Bennett, N.R., Brenan, J.M., and Fei, Y. (2016) Thermometry of the magma ocean: Controls on the metal–silicate partitioning of gold. Geochimica et Cosmochimica Acta, 184, 173-192.

Berthet, S., Malavergne, V., and Righter, K. (2009) Melting of the Indarch meteorite (EH4 chondrite) at 1 GPa and variable oxygen fugacity: Implications for early planetary differentiation processes. Geochimica et Cosmochimica Acta, 73(20), 6402-6420.

Blanchard, I., Siebert, J., Borensztajn, S., and Badro, J. (2017) The solubility of heat-producing elements in Earth's core. Geochemical Perspectives Letters, 5, 1-5.

Blundy, J., Wood, B.J., 2003. Mineral-Melt Partitioning of Uranium, Thorium and Their Daughters. Reviews in Mineralogy and Geochemistry 52, 59-123.

Bouhifd, M.A., Andrault, D., Bolfan-Casanova, N., Hammouda, T., and Devidal, J.-L. (2013) Metal-silicate partitioning of Pb and U: Effects of metal composition and oxygen fugacity. Geochimica et Cosmochimica Acta, 114, 13-28.

Bouhifd, M.A., Gautron, L., Bolfan-Casanova, N., Malavergne, V., Hammouda, T., Andrault, D., and Jephcoat, A.P. (2007) Potassium partitioning into molten iron alloys at high-pressure: Implications for Earth's core. Physics of The Earth and Planetary Interiors, 160(1), 22-33.

Bouhifd, M.A., and Jephcoat, A.P. (2011) Convergence of Ni and Co metal-silicate partition coefficients in the deep magma-ocean and coupled silicon-oxygen solubility in iron melts at high pressures. Earth and Planetary Science Letters, 307(3-4), 341-348.

Boujibar, A., Andrault, D., Bouhifd, M.A., Bolfan-Casanova, N., Devidal, J.-L., and Trcera, N. (2014) Metal–silicate partitioning of sulphur, new experimental and thermodynamic constraints on planetary accretion. Earth and Planetary Science Letters, 391(0), 42-54.

Cartier, C., Hammouda, T., Boyet, M., Bouhifd, M.A., and Devidal, J.-L. (2014) Redox control of the fractionation of niobium and tantalum during planetary accretion and core formation. Nature Geoscience, 7, 573-576.

Chabot, N.L., and Drake, M.J. (1999) Potassium solubility in metal: the effects of composition at 15 kbar and 1900ºC on partitioning between iron alloys and silicate melts. Earth & Planetary Science Letters, 172.

Chabot, N.L., Wollack, E.A., Klima, R.L., and Minitti, M.E. (2014) Experimental constraints on Mercury's core composition. Earth and Planetary Science Letters, 390(0), 199-208.

Chidester, B.A., Rahman, Z., Righter, K., and Campbell, A.J. (2017) Metal–silicate partitioning of U: Implications for the heat budget of the core and evidence for reduced U in the mantle. Geochimica et Cosmochimica Acta, 199, 1-12.

Corgne, A., Keshav, S., Fei, Y., and McDonough, W.F. (2007) How much potassium is in the Earth's core? New insights from partitioning experiments. Earth & Planetary Science Letters, 256, 567-576.

Corgne, A., Keshav, S., Wood, B.J., McDonough, W.F., and Fei, Y. (2008) Metal–silicate partitioning and constraints on core composition and oxygen fugacity during Earth accretion. Geochimica et Cosmochimica Acta, 72(2), 574-589.

32

Dreibus, G., and Wänke, H. (1985) Mars, a volatile-rich planet. Meteoritics, 20(2), 367-381.

Filiberto, J., Treiman, A.H., and Le, L. (2008) Crystallization experiments on a Gusev Adirondack basalt composition. Meteoritics & Planetary Science, 43(7), 1137-1146.

Fischer, M., Lahmar, A., Maglione, M., San Miguel, A., Itié, J.P., Polian, A., and Baudelet, F. (1994) Local disorder studied in $SrTiO_3$ at low temperature by EXAFS spectroscopy. Physical Review B, 49(18), 12451-12456.

Fischer, R.A., Campbell, A.J., Reaman, D.M., Miller, N.A, Heinz D.L., Dera P., Prakapenka, VB. (2013) Phase relations in the Fe–FeSi system at high pressures and temperatures. Earth & Planetary Science Letters, 373, 54-64.

Fischer, R.A., Nakajima, Y., Campbell, A.J., Frost, D.J., Harries, D., Langenhorst, F., Miyajima, N., Pollok, K., and Rubie, D.C. (2015) High pressure metal–silicate partitioning of Ni, Co, V, Cr, Si, and O. Geochimica et Cosmochimica Acta, 167, 177-194.

Hauck II, S.A., Margot, J.-L., Solomon, S.C., Phillips, R.J., Johnson, C.A., Lemoine, F.G., Mazarico, E., McCoy, T.J., Padovan, S., Peale, S., Perry, M.E., Smith, D.E., and Zuber, M.T. (2013) The curious case of Mercury's internal structure. JGR: Planets, 118, 1-17.

Huebner, J.S. (1971) Buffering Techniques for Hydrostatic Systems at Elevated Pressures. In G.C. Ulmer, Ed. Research Techniques for High Pressure and High Temperature, p. 123-177. Springer Berlin Heidelberg, Berlin, Heidelberg.

Knibbe, J.S., van Westrenen, W. (2018) The interior configuration of planet Mercury constrained by moment of inertia and planetary contraction. JGR: Planets, 120, 1904–1923.

la Tourrette, T., and Wasserburg, G.J. (1997) Self diffusion of europium, neodymium, thorium, and uranium in haplobasaltic melt: The effect of oxygen fugacity and the relationship to melt structure. Geochimica et Cosmochimica Acta, 61(4), 755-764.

Liebske, C. (2005) Mantle melting at high pressure -Experimental constraints on magma ocean differentiation. Bayerishes GeoInstitut, p. 220. University of Bayreuth, Bayreuth.

Liu, J., Li, J., and Ikuta, D. (2016) Elastic softening in Fe7C3 with implications for Earth's deep carbon reservoirs. Journal of Geophysical Research: Solid Earth, 121(3), 1514-1524.

Lodders, K., and Fegley, B. (1998). The Planetary Scientist's Companion. Oxford Univ. Press, New York.

Lodders, K. (2003). Solar System abundances and condensation temperatures of the elements. The Astrophysical Journal, 591, 1220–1247.

Ma, Z. (2001) Thermodynamic Description for Concentrated Metallic Solutions Using Interaction Parameters. Metallurgical and materials transactions B, 32B, 87-103.

Malavergne, V., Tarrida, M., Combes, R., Bureau, H., Jones, J., and Schwandt, C. (2007) New high-pressure and high-temperature metal/silicate partitioning of U and Pb: Implications for the cores of the Earth and Mars. Geochimica et Cosmochimica Acta, 71, 2637-2655.

Malavergne, V., Toplis, M., J., Berthet, S., and Jones, J. (2010) Highly reducing conditions during core formation on Mercury: Implications for internal structure and the origin of a magnetic field. Icarus, 206, 199-209.

McCubbin, F.M., Riner, M.A., Vander Kaaden, K.E., and Burkemper, L.K. (2012) Is Mercury a volatile-rich planet? Geophysical Research Letters, 39(9), L09202.

McCubbin, F.M., Vander Kaaden, K.E., Peplowski, P.N., Bell, A.S., Nittler, L.R., Boyce, J.W., Evans, L.G., Keller, L.P., Elardo, S.M., and McCoy, T.J. (2017) A Low O/Si Ratio on the Surface of Mercury: Evidence for Silicon Smelting? Journal of Geophysical Research: Planets, 122(10), 2053-2076.

McDonough, W.F., Sun, S.-S., Ringwood, A.E., Jagoutz, E., and Hofmann, A.W. (1992) Potassium, rubidium, and cesium in the Earth and Moon and the evolution of the mantle of the Earth. Geochimica et Cosmochimica Acta, 56, 1001-1012.

33

McDonough, W.F., and Sun, S.S. (1995) The composition of the Earth. Chemical Geology, 120, 223-253.

Mills, N.M., Agee, C.B., and Draper, D.S. (2007) Metal-silicate partitioning of cesium: Implications for core formation. Geochimica et Cosmochimica Acta, 71, 4066-4081.

Morard, G., and Katsura, T. (2010) Pressure–temperature cartography of Fe–S–Si immiscible system. Geochimica et Cosmochimica Acta, 74(12), 3659-3667.

Morard, G., Siebert, J. and Badro, J. (2014) Partitioning of Si and platinum group elements between liquid and solid Fe-Si alloys. Geochimica Cosmochimica Acta, 132, 94-100.

Namur, O., Charlier, B., Holtz, F., Cartier, C., and McCammon, C. (2016a) Sulfur solubility in reduced mafic silicate melts: Implications for the speciation and distribution of sulfur on Mercury. Earth & Planetary Science Letters, 448, 102-114.

Namur, O., Collinet, M., Charlier, B., Grove, T.L., Holtz, F., and McCammon, C. (2016b) Melting processes and mantle sources of lavas on Mercury. Earth & Planetary Science Letters, 439, 117-128.

Nishida, K., Terasaki, H., Ohtani, E., and Suzuki, A. (2008) The effect of sulfur content on density of the liquid Fe–S at high pressure. Physics and Chemistry of Minerals, 35(7), 417-423.

Nittler, L.R., Chabot, N., Grove, T.L., and Peplowski, P.N. (2018) The Chemical Composition of Mercury. In B.J. Anderson, L.R. Nittler, and S.C. Solomon, Eds. Mercury: The View after MESSENGER, p. 30-51. Cambridge University Press, Cambridge.

Nittler, L.R., McCoy, T.J., Clark, P.E., Murphy, M.E., Trombka, J.I., and Jarosewich, E. (2004) Bulk element compositions of meteorites: A guide for interpreting remote-sensing geochemical measurements of planets and asteroids. Antartic Meteorite Research, 17, 231.

Norman, M.D., Pearson, N.J., Sharma, A., and Griffin, W.L. (1996) Quantitative analysis of trace elements in geological materials by laser ablation ICPMS: Instrumental operating conditions ans calibration values of NIST glasses. Geostandards and geoanalytical research, 20(2), 247-261.

O'Neill, H.S.C., and Eggins, S.M. (2002) The effect of melt composition on trace element partitioning: an experimental investigation of the activity coefficients of FeO, NiO, CoO, MoO2 and MoO3 in silicate melts. Chemical Geology, 186(1–2), 151-181.

O'Neill, H.S.C., and Palme, H. (1998) Composition of the silicate Earth: implications for accretion and core formation. Cambridge University Press.

Padovan, S., Wieczorek, M.A., Margot J.-L., Tosi, N., and Solomon, S.C. (2015) Thickness of the crust ofMercury from geoid-to-topography ratios. Geophysical Research Letters, 42, 1029–1038.Pearce, N.J.G., Perkins, W.T., and Westgate, J.A. (1997) A Compilation of New and Published Major and Trace Element Data for NIST SRM 610 and NIST SRM 612 Glass Reference Materials. Geostandards and geoanalytical research, 21, 115-144.

Peplowski, P.N., Evans, L.G., Hauck II, S.A., McCoy, T.J., Boynton, W.V., Gillis-Davis, J.J., Ebel, D.S., Goldsten, J.O., Hamara, D.K., Lawrence, D.J., McNutt, R.L., Nittler, L.R., Solomon, S.C., Rhodes, E.A., Sprague, A.L., Starr, R.D., and Stockstill-Cahill, K.R. (2011) Radioactive Elements on Mercury's Surface from MESSENGER: Implications for the Planet's Formation and Evolution. Science333, 1850-1852.

Ricolleau, A., Fei, Y., Corgne, A., Siebert, J., and Badro, J. (2011) Oxygen and silicon contents of Earth's core from high pressure metal–silicate partitioning experiments. Earth & Planetary Science Letters, 310, 409-421.

Righter, K. (2003) Metal-silicate partitioning of siderophile elements and coreformation in the early Earth. Annual Review of Earth and Planetary Sciences, 31, 135-174.

Righter, K., Humayun, M., and Danielson, L. (2008) Partitioning of palladium at high pressures and temperatures during core formation. Nature Geoscience, 1(5), 321-323.

Robie, R.A., and Hemingway, B.S. (1995) Thermodynamic properties of minerals and related substances at 298.15°K and 1 Bar (105 Pascals) pressure and at higher temperatures. 461 p. USGS.

Rubie, D.C., Gessmann, C.K., and Frost, D.J. (2004) Partitioning of oxygen during core formation on the Earth and Mars. Nature, 429, 58-62.

Siebert, J., Badro, J., Antonangeli, D., and Ryerson, F.J. (2012) Metal-silicate partitioning of Ni and Co in a deep magma ocean. Earth & Planetary Science Letters, 321-322, 189-197.

Smith, D.E., Zuber, M.T., Phillips, R.J., Solomon, S.C., Hauck, S.A., Lemoine, F.G., Mazarico, E., Neumann, G.A., Peale, S.J., Margot, J.-L., Johnson, C.L., Torrence, M.H., Perry, M.E., Rowlands, D.D., Goossens, S., Head, J.W., and Taylor, A.H. (2012) Gravity Field and Internal Structure of Mercury from MESSENGER. Science, 336(6078), 214-217.

Sori, M.M. (2018) A thin, dense crust for Mercury. Earth & Planetary Science Letters, 489, 92-99.

Steenstra, E.S., Agmon, N., Berndt, J., Klemme, S., Matveev, S., and van Westrenen, W. (2018) Depletion of potassium and sodium in mantles of Mars, Moon and Vesta by core formation. Scientific Reports, 8(1), 7053.

Suer, T.-A., Siebert, J., Remusat, L., Menguy, N., and Fiquet, G. (2017) A sulfur-poor terrestrial core inferred from metal–silicate partitioning experiments. Earth and Planetary Science Letters, 469, 84-97.

Tateyama, R., Ohtani, E., Terasaki, H., Nishida, K., Shibazaki, Y., Suzuki, A., and Kikegawa, T. (2011) Density measurements of liquid Fe–Si alloys at high pressure using the sink–float method. Physics and Chemistry of Minerals, 38(10), 801-807.

Tosi, N., Grott, M., Plesa, A.-C., and Breuer, D. (2013) Thermochemical evolution of Mercury's interior. Journal of Geophysical Research: Planets, 118(12), 2474-2487.

Tsuno, K., Frost, D.J., and Rubie, D.C. (2013) Simultaneous partitioning of silicon and oxygen into the Earth's core during early Earth differentiation. Geophysical Research Letters, 40, 66-71.

Tuff, J., Wood, B.J., and Wade, J. (2011) The effect of Si on metal-silicate partitioning of siderophile elements and implications for the conditions of core formation. Geochimica et Cosmochimica Acta, 75, 673-690.

Turcotte, D.L. and Schubert, G. (2002) Geodynamics, 2nd ed. 456 pp. Cambridge University Press.Wade, J., Wood, B.J., and Tuff, J. (2012) Metal–silicate partitioning of Mo and W at high pressures and temperatures: Evidence for late accretion of sulphur to the Earth. Geochimica et Cosmochimica Acta, 85, 58-74.

Wänke, H., Baddenhausen, H., Dreibus, G., Jagoutz, E., Kruse, H., Palme, H., Spettel, B., and Teschke, F. (1973) Multielement analyses of Appolo 15, 16 and 17 samples and the bulk composition of the moon. Proc. Lunar Planet. Sci. Conf., 2, 1461-1481.

Wasson, J.T., and Kallemeyn, G.W. (1988) Composition of chondrites. Philosophical Transaction of the Royal Society of London, A325, 535-544.

Wohlers, A., and Wood, B.J. (2015) A Mercury-like component of early Earth yields uranium in the core and high mantle ^{142}Nd. Nature, 520, 337-340.

Wohlers, A., and Wood, B.J. (2017) Uranium, thorium and REE partitioning into sulfide liquids: Implications for reduced S-rich bodies. Geochimica et Cosmochimica Acta, 205, 226-244.

Zolotov, M.Y., Sprague, A.L., Hauck II, S.A., Nittler, L.R., Solomon, S.C., and Weider, S.Z. (2013) The redox state, FeO content, and origin of sulfur-rich magmas on Mercury. JGR : Planets, 118, 138-146.

Figure captions

Figure 1:

Textures and coexisting phases in experimental charges. Backscattered electron images of samples #1000 (A), #975 (B & C), #904 (D & E), #907 (F) and PR1578 (G). All samples contain segregated silicate melt and Si-rich metal. Some samples also contain orthopyroxene crystals (opx) (D) and Fe sulfide which comprises quenched microstructures (B & C). A few samples contain euhedral U-Th oxides crystallized at high temperature (E, F) and dendritic Si metal crystals formed during the quench (G) (see text for more details). Circles in (C) show an example set of analyses in a sulfide blob. In (D) and (E), sample #904 is shown in the same location, by varying the brightness and contrast to show the lightest (opx) and heaviest (U-Th-oxides) phases.

Figure 2:

Experimental partitioning coefficients of U, Th and K between metal and silicate (white symbols) and between sulfide and silicate (black symbols), as a function of oxygen fugacity. Data are shown for this study and previously published studies (Bouhifd et al., 2013; Bouhifd et al., 2007; Chabot and Drake, 1999; Corgne et al., 2007; Malavergne et al., 2007; Mills et al., 2007; Steenstra et al., 2018; Wohlers and Wood, 2015; Wohlers and Wood, 2017). U, Th and K become more siderophile and chalcophile with decreasing oxygen fugacity, and their affinities with sulfides are stronger than with metals. However, these effects are weaker for K than U and Th.

Figure 3:

Comparison between measured and predicted partition coefficients of U, Th and K between metal and silicate (left) and between sulfide and silicate (right). Solid lines and dotted lines

36

represent the 1:1 correspondence and the 1σ error of the linear regression (Eq. 13-14 in main text). For the linear regressions, we used selected data from those shown in Fig. 2, where O concentration was measured in metal and sulfide phases.

Figure 4:

Corrected experimental partitioning coefficients of U, Th and K between sulfide and silicate (A) and between metal and silicate (B). Data are the same as those shown in Fig. 3. Partition coefficients are corrected from initial values using Eq. (13-14), in order to isolate the effects of each parameter shown on the x axis. We fixed all other parameters to values used in the model of Mercury's differentiation at IW-5.5 (see discussion for more details and Table 4 for assumed core and sulfide composition). Solid and dotted lines are calculated partition coefficients using Eq. (13-14) and propagated 1σ errors associated with each parameter. The yellow diamonds show partition coefficients resulting from the model of Mercury's differentiation at IW -5.5.

Figure 5 A: Comparison between measured and predicted O concentration in metals and sulfides (wt%). Solid line and dotted lines represent the 1:1 correspondence and the 1σ error of the linear regression (Eq. 22). Used data for the fit are from (Asahara et al., 2004; Bouhifd et al., 2007; Bouhifd and Jephcoat, 2011; Boujibar et al., 2014; Corgne et al., 2007; Corgne et al., 2008; Fischer et al., 2015; Mills et al., 2007; Ricolleau et al., 2011; Rubie et al., 2004; Siebert et al., 2012; Steenstra et al., 2018; Suer et al., 2017; Tsuno et al., 2013; Wohlers and Wood, 2015; Wohlers and Wood, 2017). B: Comparison between measured and calculated partition coefficient of Si between metal and silicate. Solid line and dotted lines represent the 1:1 correspondence and the 1σ error of the linear regression (Eq. 16). Regressions were performed using data from this study, (Bouhifd and Jephcoat, 2011; Boujibar et al., 2014;

37

Cartier et al., 2014; Chabot et al., 2014; Chidester et al., 2017; Fischer et al., 2015; Ricolleau et al., 2011; Siebert et al., 2012; Suer et al., 2017; Tsuno et al., 2013; Tuff et al., 2011).

Figure 6:

Measured experimental data on Si content in liquid metal (wt%) as a function of oxygen fugacity (A), shown for experiments at relatively constant pressure conditions (from this study, (Boujibar et al., 2014; Cartier et al., 2014; Chabot et al., 2014; Ricolleau et al., 2011; Tsuno et al., 2013). Variation of C (B) and S contents (C) as a function of Si content in the metal (wt%) for experimental data from Cartier et al. (2014) conducted at 5 GPa. Modeled core compositions for each considered fO_2 are also shown in (B) and (C) as yellow diamonds (see text for more details). In A, Si content in Mercury's core is slightly higher than experiments, due to a lower bulk Si content of experimental samples.

Figure 7:

Calculated bulk sulfur content (A) and Fe/Si ratio (B) in Mercury based on our models of Mercury's differentiation (see text for more details) as a function of the oxygen fugacity and the mass fraction of any existing FeS layer between the core and mantle. We only considered the presence of a sulfide layer for models of fO_2 comprised between IW-5.5 and IW-4, because metal-sulfide immiscibility is not expected at higher fO_2 and we only extrapolated sulfide-silicate partitioning of HPE down to IW-5.5 (see text for more details). A: For all models, the magma ocean is considered as saturated in S (see text for more details and Table 4 for S concentration in bulk silicate Mercury). At a fO_2 higher than IW-4, bulk sulfur content is controlled by its concentration in the core and BSM. At lower fO_2, S concentration in the core is very low (Table 4), and its bulk planetary concentration is therefore controlled by its abundance in BSM and the possible sulfide layer. Since S solubility in the silicate increases with decreasing fO_2, for any fixed bulk S content, lower fO_2 yields higher S in BSM and a

38

thinner sulfide layer. B: Fe/Si ratio decreases with decreasing fO_2, because Si becomes more siderophile at reduced conditions. For comparison, we show ranges of bulk sulfur contents in chondrites compiled in (Nittler et al., 2004). CC: Carbonaceous chondrites, EC: Enstatite chondrites, OC: Ordinary chondrites. Our results show that for certain ranges of fO_2 and thickness of the sulfide layer, bulk Mercury S and Fe/Si can be chondritic.

Figure 8:

Bulk Mercury K/U (A) and K/Th (B) ratios calculated for an equilibration between core and mantle from IW-2.6 to IW-5.5 (colors in legend) as a function of the thickness of the FeS layer from 0 to 15 wt% (0 to ~204 km thickness). Ratios for surfaces of Mercury (Peplowski et al., 2011) and Venus (Lodders and Fegley, 1998) and bulk silicate Earth (McDonough and Sun, 1995) and Mars (Dreibus and Wänke, 1985) are shown for comparison.

Figure 9:

K/U and K/Th for terrestrial planets as a function of the heliocentric distance (A & B respectively). Surface, and bulk silicate values of other terrestrial planets are shown with bulk ratios calculated for Mercury for two cases: core segregation at IW-5.5 and a sulfide layer 204 km thick (dark blue squares) and core segregation at IW-4 with no sulfide layer (orange squares). The first scenario at IW-5.5 yields a correlation of K/U ratio with the heliocentric distance in agreement with previous models of volatile depletion in the inner Solar System (Albarède, 2009) and a K/Th ratio close to Venus' and Earth's values. The second less reduced scenario yields bulk ratios similar to those measured on the surface and point to an enrichment of Mercury in K relatively to previously expected values. Chondritic ratios are also shown for comparison (Wasson and Kallemeyn, 1988).

Figure 10:

Radioactive heat production by the decay of ^{238}U, ^{235}U, ^{232}Th and ^{40}K in bulk Mercury at the present time, as a function of the thickness of the possible sulfide layer, considering a mantle free of HPE or with concentrations equivalent to 20% those measured on the surface. In case of the absence of a sulfide layer, changing the fO_2 of Mercury's differentiation affects weakly radioactive heat generation. In our models, since we consider that the sulfide layer thickens at the expense of the mantle and total HPE are less concentrated in sulfides than in the silicate, total heat budget decreases with the thickness of the sulfide layer.

Appendix

Supplementary Material related to this article can be found online. It contains supplementary

tables giving chemical compositions of coexisting phases in our samples.

Tables

Table 1: Chemical compositions of the starting materials.

Metal (wt%)

U-Th-bearing samples	Fe	Ni	Co	S	Si
U-Th-1	75.8	4.2	0.2	11.8	8.0
U-Th-2	71.1	3.9	0.2	11.1	13.7
U-Th-3	66.8	3.7	0.2	10.4	19.0
U-Th-4	60.0	3.3	0.1	9.3	27.1
U-Th-5	61.8	4	0.18	20	14
U-Th-6	56.4	4	0.18	25.5	14
U-Th-7	36.4	2.6	0	16.4	44.6
U-Th-8	38.1	2.4	0	11.8	49.5

K-bearing samples	Fe	Ni	Co	S	Si
K-1	75.8	4.2	0.2	11.8	8
K-2	72.0	4.0	0.2	11.2	12.6
K-3	67.3	3.7	0.2	10.5	18.3
K-4	62.9	3.5	0.2	9.8	23.7
K-5	57.5	3.2	0.1	9.0	30
K-6	56.4	4	0.2	25.5	14
K-7	37.4	0	0	16.9	45.7
K-8	37.3	0	0	12.1	50.7

Silicate (wt%)	SiO_2	MgO	Al_2O_3	CaO	Na_2O	K_2O	Cr_2O_3	MnO_2	TiO_2	UO_2	ThO_2	FeO
U-Th-bearing samples	52.8	33.2	2.8	1.8	1.9	0.2	0.9	0.6	0.1	2.9	2.9	0
K-bearing samples1	46.7	29.4	2.4	1.6	1.7	16.7	0.8	0.5	0.1	0	0	0
K-bearing samples2*	49.68	9.46	12.7	10.79	0	15	0	0	0	0	0	11.05

* Samples PR1577 and PR1578 (Table 2) were performed using the silicate composition shown for K-bearing samples2. All other samples had a starting silicate composition of K-bearing samples1 for the K-series of samples and U-Th-bearing samples for the U-Th series of samples.

Table 2: Experimental conditions, coexisting phases and partition coefficients.

Run no. / K-bearing samples	Starting material	T (°C)	P (GPa)	Time (min)	log fO_2 (relative to IW)	Metal	Sulfide	Silicate Melt	Opx	St	U-Th-oxides		log D_K	σ		
#922	K-1	1650	1	90	-1.78	X		X	X			Met/sil	-1.8	0.62		
#925	K-1	1700	1	45	-1.81	X		X				Met/sil	-1.79	0.22		
#306	K-4	1900	5	5	-2.25	X	X	X				Met/sil	-3.87	0.3		
												Sulf/sil	-2.57	0.25		
#921	K-1	1600	1	90	-2.3	X	X	X	X			Met/sil	-1.76	0.21		
#919	K-1	1550	1	180	-2.33	X	X	X	X			Met/sil	-2.11	0.06		
#916	K-1	1500	1	210	-2.42	X		X	X			Met/sil	-1.79	0.16		
#1027	K-6	1700	1	45	-2.83	X	X	X				Met/sil	-2.03	0.18		
												Sulf/sil	-1.5	0.28		
#1026	K-4	1700	1	50	-2.95	X	X	X				Met/sil	-1.82	0.14		
												Sulf/sil	-1.52	0.21		
#999	K-2	1700	1	45	-3.46	X	X	X				Met/sil	-1.69	0.2		
#1001	K-3	1700	1	45	-4.46	X		X				Met/sil	-3	0.27		
#1029	K-5	1700	1	50	-4.52	X		X				Met/sil	-2.47	0.11		
#1000	K-4	1700	1	45	-4.96	X		X				Met/sil	-2.84	0.16		
PR1577	K-7	1800	3.5	10	-6.46	X		X		X		Met/sil	-2.85	0.35		
PR1578	K-8	1800	3.5	4	-6.05	X		X		X		Met/sil	-2.79	0.32		
U-Th-bearing samples													**log D_U**	**σ**	**log D_{Th}**	**σ**
#924	U-Th-1	1650	1	90	-2.38	X	X	X	X		X	Met/sil	-4.62	0.08	-3.41	0.15
#923	U-Th-1	1700	1	45	-2.58	X		X				Met/sil	-4.51	0.21	-4.99	0.01
#910	U-Th-1	1580	1	120	-2.65	X	X	X				Met/sil	-4.05	0.31	-4.62	0.31
#907	U-Th-1	1550	1	140	-2.8	X	X	X	X		X	Met/sil	-3.53	0.51	-3.77	0.18
#974	U-Th-5	1700	1	45	-3.16	X	X	X				Met/sil	-3.28	0.48	-4.15	0.67
												Sulf/sil	0.32	0.1	-0.83	0.12
#904	U-Th-1	1500	1	180	-3.2	X	X	X	X		X	Met/sil	-4.16	0.12	-4.01	0.19
#909	U-Th-1	1600	1	90	-3.26	X		X	X			Met/sil	-4.4	0.27	-5.34	0.04
#975	U-Th-6	1700	1	45	-3.59	X	X	X				Met/sil	-4.48	0.41	-5.08	0.73
												Sulf/sil	0.32	0.14	-0.86	0.18
#420	U-Th-4	1900	3	15	-3.89	X		X				Met/sil	-2.7	0.08	-5.33	0.14
#305	U-Th-3	1900	5	5	-3.9	X	X	X				Met/sil	-4.41	0.28	-2.99	0.52
												Sulf/sil	0.4	0.15	-0.88	0.23
#967	U-Th-2	1700	1	45	-4.29	X		X				Met/sil	-3.21	0.22	-3.96	0.85
#1030	U-Th-4	1700	1	45	-4.52	X		X				Met/sil	-2.25	0.09	-4.85	0.16
#972	U-Th-4	1700	1	45	-5.23	X		X				Met/sil	-2.3	0.1	-5.08	0.13
PR1527	U-Th-7	1900	3.5	5	-5.37	X		X	X			Met/sil	-3.3	0.16	-5.67	0.04

43

Table 3: Fitted parameters for linear regressions predicting partition coefficients of U, Th and K between metal and silicate and between sulfide and silicate, and partitioning of Si and O between metal (and sulfide for O) and silicate (see text for more details).

		a	b (1/T)	c (P/T)	d (ΔIW or log(FeO))[a]	e (log(1-X_S)/T)	f (log(1-X_C)/T)	g (log(1-X_{Si})/T)	h (log(1-X_O)/T)	i (nbo/t)	j(log(1-xSsil)/T)	k(ΔIW^2)	N[b]	σ	R²	F	p-value
U (met/sil)	Coefficient	-0.3393	-10300	[c]	-0.5				-89.09				39	0.5105	0.9473	324	9E-24
	σ	0.4431	911						14.75								
	P-value	5E-01	2E-13						6E-07								
U (sulf/sil)	Coefficient	-0.8795	7014		-1	19.29	49.65		-46.69	-0.5879	-48.07		25	0.3227	0.843	16	2E-06
	σ	0.7507	3523			8.66	21.61		18.24	0.1721	5.97						
	P-value	0.26	0.06			2E-05	2E-05		1E-05	3E-03	1E-10						
Th (met/sil)	Coefficient	-5.918			-0.5	-83.46			90.01	-0.5652			22	0.7036	0.4974	6	5E-03
	σ	0.4				38.07			39.51	0.2916							
	P-value	2E-11				4E-02			4E-02	7E-02							
Th (sulf/sil)	Coefficient	0.3749	-5133		-1		61.26	335.1	-133.4	-0.5718	-68.56		25	0.231	0.9476	54	2E-10
	σ	0.5824	1000				16.37	55.1	12.9	0.1084	4.61						
	P-value	5E-01	7E-05				2E-03	1E-05	5E-09	5E-05	2E-11						
K (met/sil)	Coefficient	-3.08			-0.25	10.79	24.21	12.83		0.3855			40	0.3726	0.7117	22	5E-09
	σ	0.2056				5.62	8.27	1.74		0.103							
	P-value	9E-17				6E-02	6E-03	1E-08		7E-04							
K (sulf/sil)	Coefficient	-0.5461	-6936		-0.5	-14.24		232.2	-53.68	0.1678	9.039		42	0.1844	0.8844	45	6E-15
	σ	0.393	715			1.76		60.9	6.97	0.0537	2.944						
	P-value	2E-01	2E-11			2E-09		5E-04	5E-09	4E-03	4E-03						
Si (met/sil) (>IW-4.5)	Coefficient	-2.51	-4074	47.83	-1				-51.27	-0.1503			137	0.3717	0.8551	195	2E-54
	σ	0.5019	875.3	15.66					8.16	0.0393							
	P-value	2E-06	8E-06	3E-03					5E-09	2E-04							
Si (met/sil) (<IW-4.5)[d]	Coefficient	-1.415	-4074	47.83	-1				-51.27	-0.1503		-0.0725	39	0.1783	0.955	785	2E-26
	σ	0.083										0.0026					
	P-value	1.00E-15										2.00E-26					
O (met/sil or sulf/sil)	Coefficient	1.856	-3461	20.07	0.5	-4.122	-5.166	-12.11					224	0.303	0.5587	55	7E-37
	σ	0.178	399	6.07		0.369	2.758	2.34									
	P-value	6.E-21	1.E-15	1.E-03		3.E-23	6.E-02	5.E-07									

[a] d term is related to ΔIW for Si and O partitioning and for U, Th and K between S-poor metals and silicate. For equilibria between sulfides and silicates d parameter is associated with log FeO (in wt%). This term was fixed to theoretical values derived from involved reactions during partitioning (see text for more details).

[b] N is the number of data used for each regression.

[c] We performed usual statistical tests (p-values) and only selected parameters that are significant at the 10% significance level.

[d] For Si partitioning between metal and silicate at very low fO_2, we fixed all parameters to those found at higher fO_2, and re-fitted intercept a and parameter k (see text for more details).
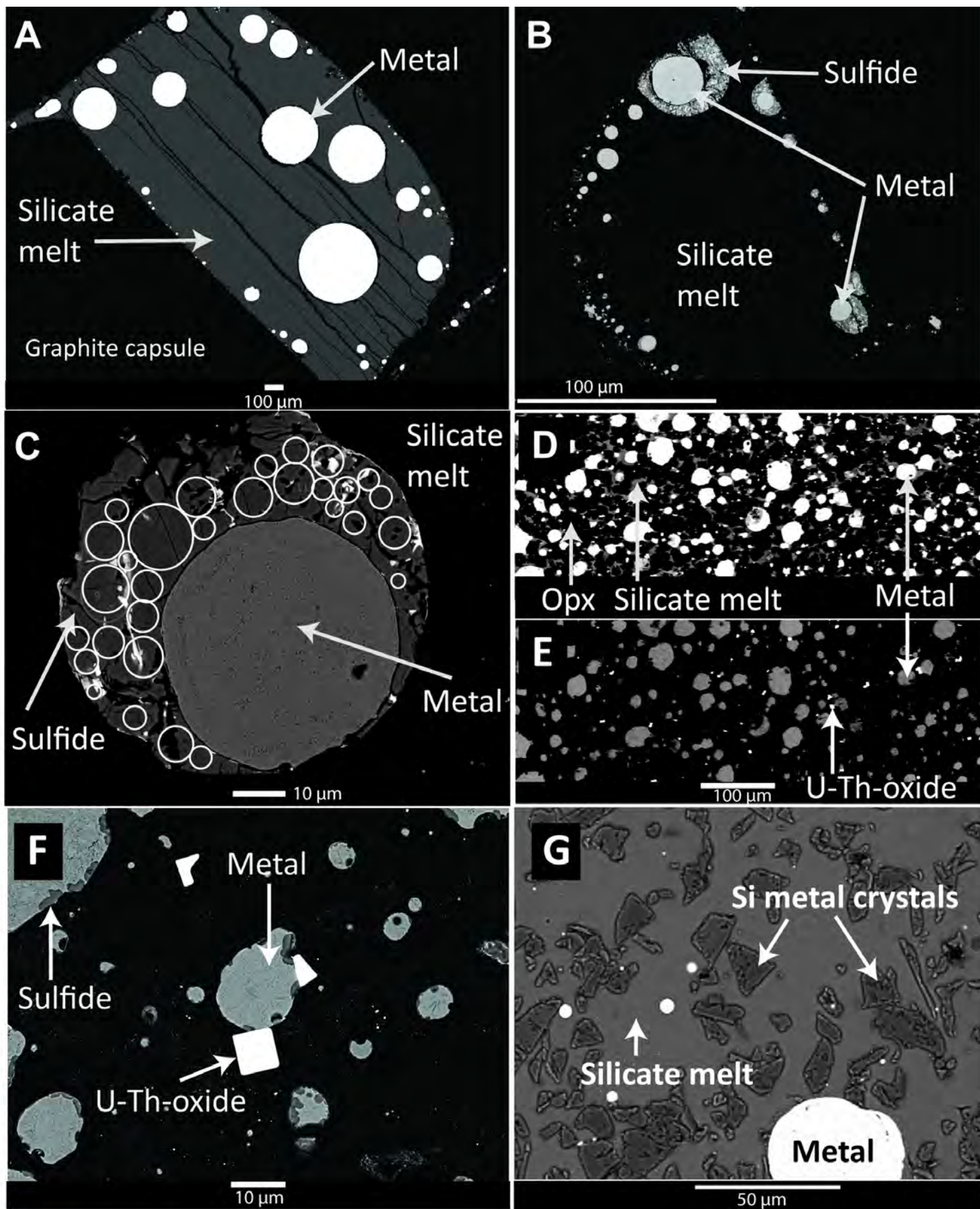
Table 4: Calculated chemical composition of Mercury's core and Fe sulfide layer, FeO and S concentrations in bulk silicate Mercury, and U, Th and K distribution coefficients between core and mantle and between sulfide and mantle.
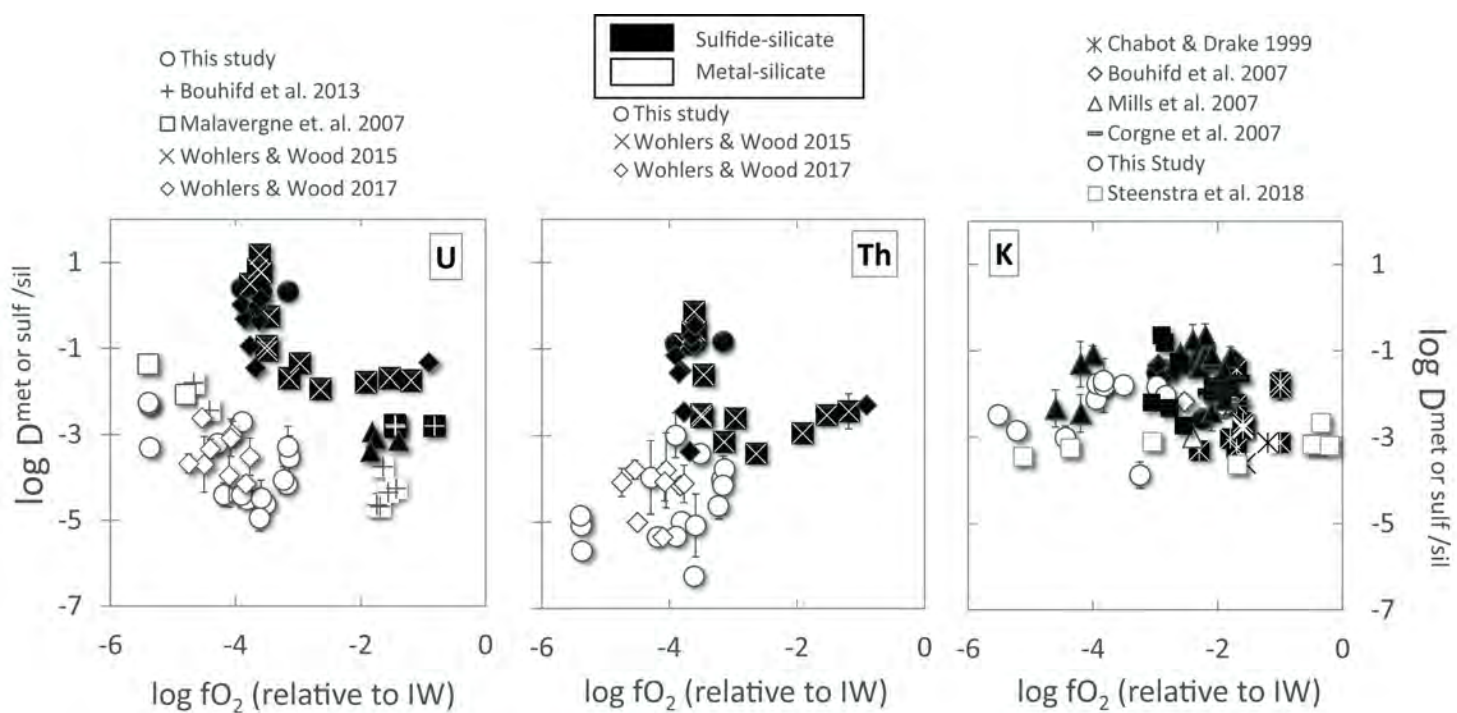
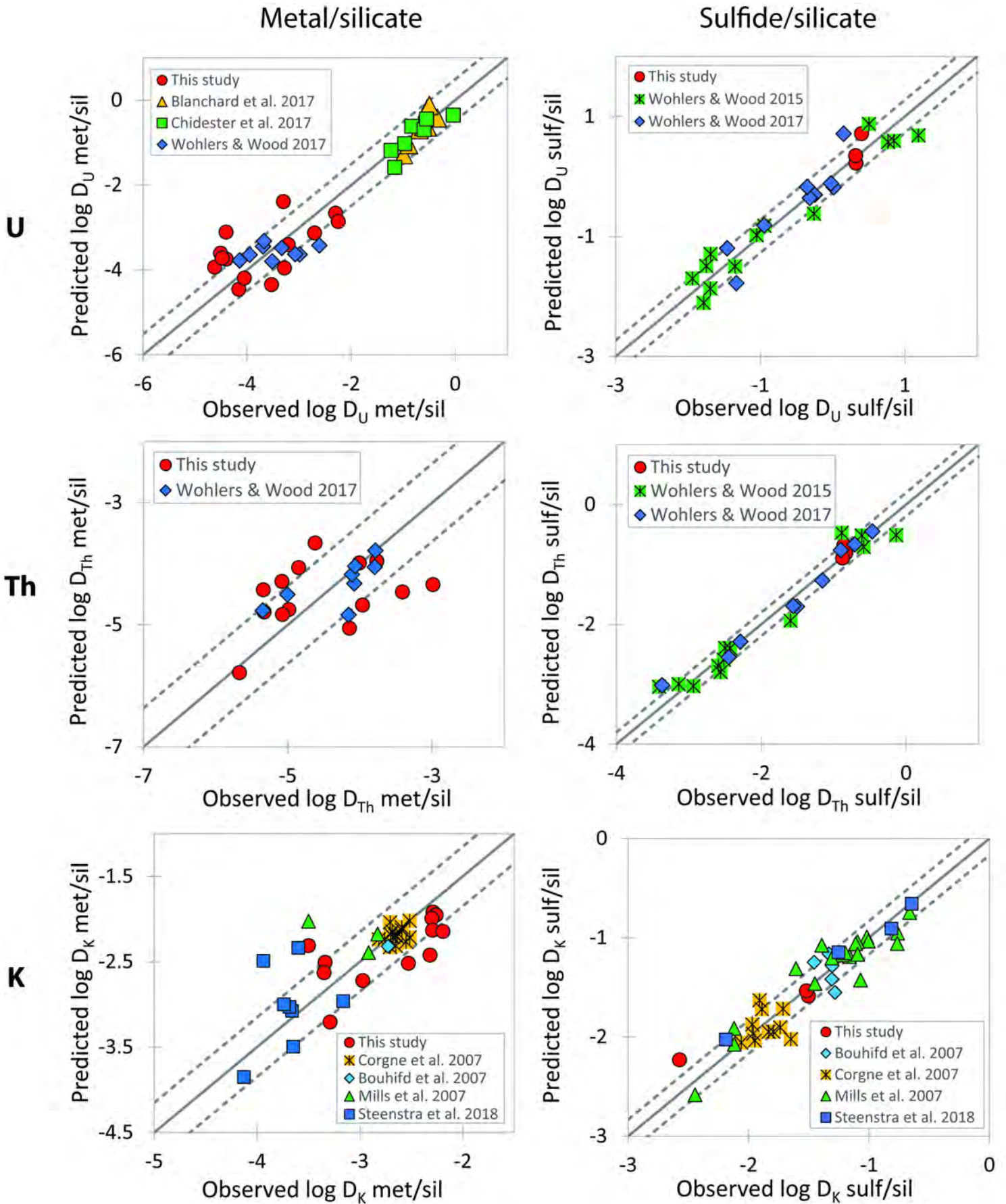| Models of Mercury's core composition	IW-7.3	IW-6	IW-5.5	IW-5	IW-4	IW-3	IW-2.6
Core composition (wt%)							
Si	65.7	59	49	37	19.3	1.93	0.77
O	0	0	0	0	0	0	0
S	0.005	0.009	0.02	0.07	0.41	2.2	2.46
C	0	0	0	0	0.83	5.85	6.18
Fe	32.4	38.8	44.6	59.5	75.2	85.2	85.7
Ni	1.9	2.22	2.55	3.40	4.30	4.87	4.90
Composition of sulfide layer (wt%)							
O			0.02	0.05	0.09		
S			35.9	35.9	35.8		
C			1	1	1		
Fe			59.7	59.7	59.7		
Ni			3.4	3.4	3.4		
FeO in Bulk Silicate Mercury (wt%)[a]	0.37	0.37	0.38	0.38	0.56	1.25	1.78
S in saturated Bulk Silicate Mercury (wt%)[b]	22.8	13.0	8.8	6.8	4.0	2.0	1.7
Log (Distribution coefficients)[c]							
U							
Core-mantle	-1.3	-2	-2.2	-2.5	-3.0	-3.5	-3.7
Sulfide-mantle			0.1	-0.2	-0.8		
Th							
Core-mantle	-3.1	-3.7	-4.0	-4.2	-4.6	-4.6	-4.7
Sulfide-mantle			-0.2	-0.8	-1.5		
K							
Core-mantle	-5.7	-5.2	-4.3	-3.4	-2.6	-2.5	-2.6
Sulfide-mantle			-1.2	-1.1	-1.0		

[a] FeO concentration in Bulk Silicate Mercury was calculated based on the fO_2 and core composition of each model and Eq. 3 (see text for more details).
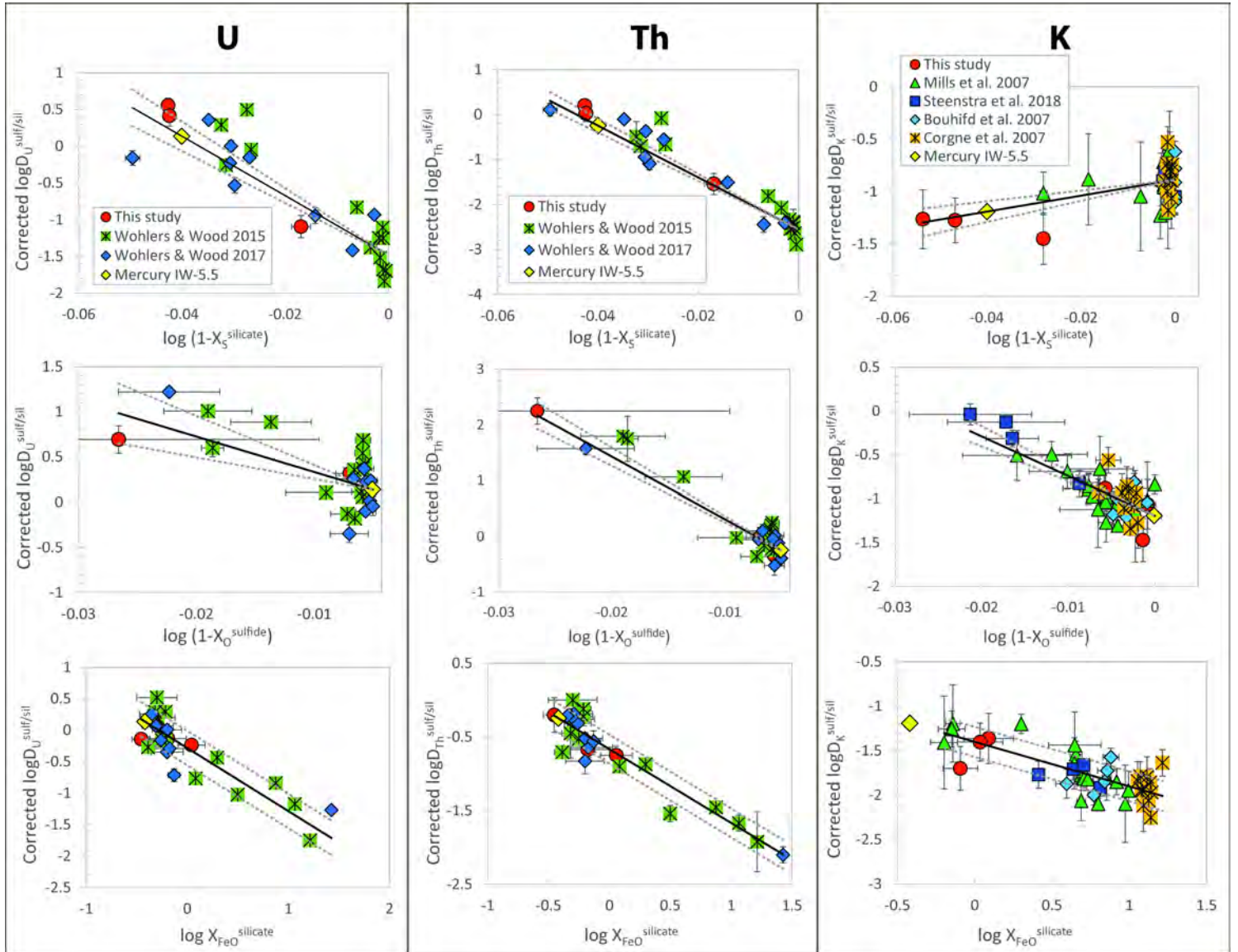
[b] Sulfur concentration in Bulk Silicate Mercury is based on S solubility in silicate melts (Namur et al. 2016a).
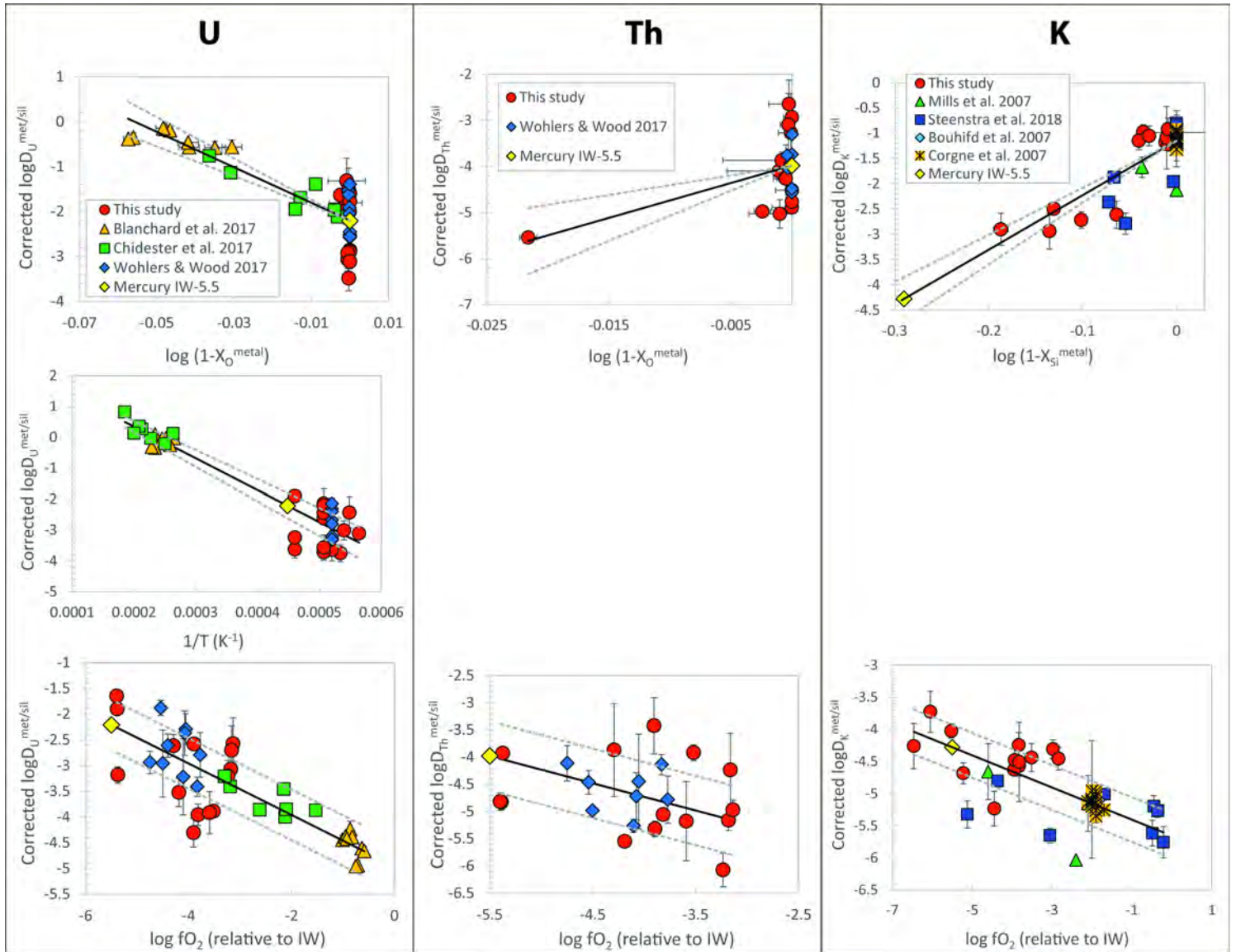
[c] Calculated distribution coefficients are for each considered fO_2, corresponding core and sulfide layer compositions and FeO and S concentrations in the bulk silicat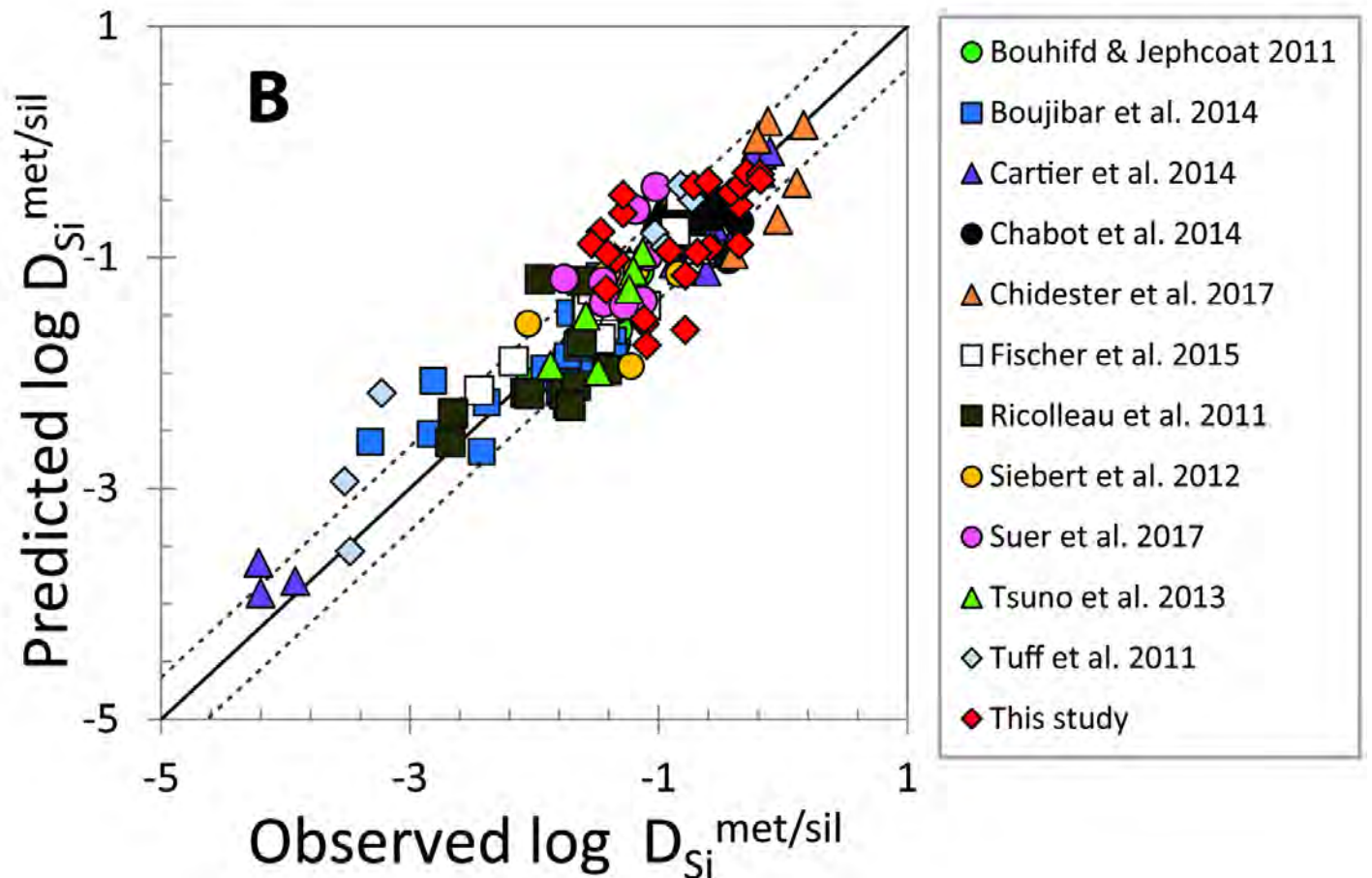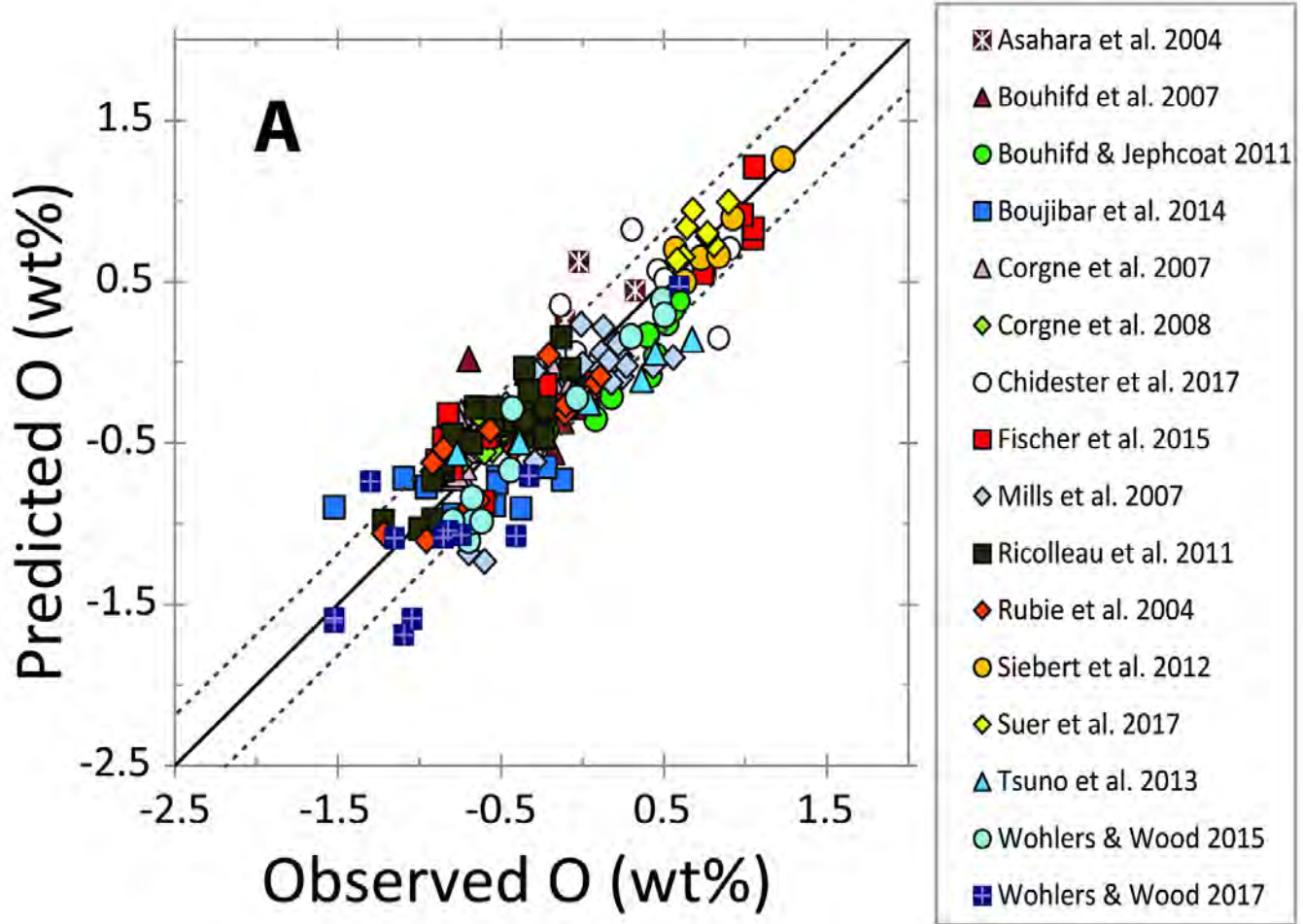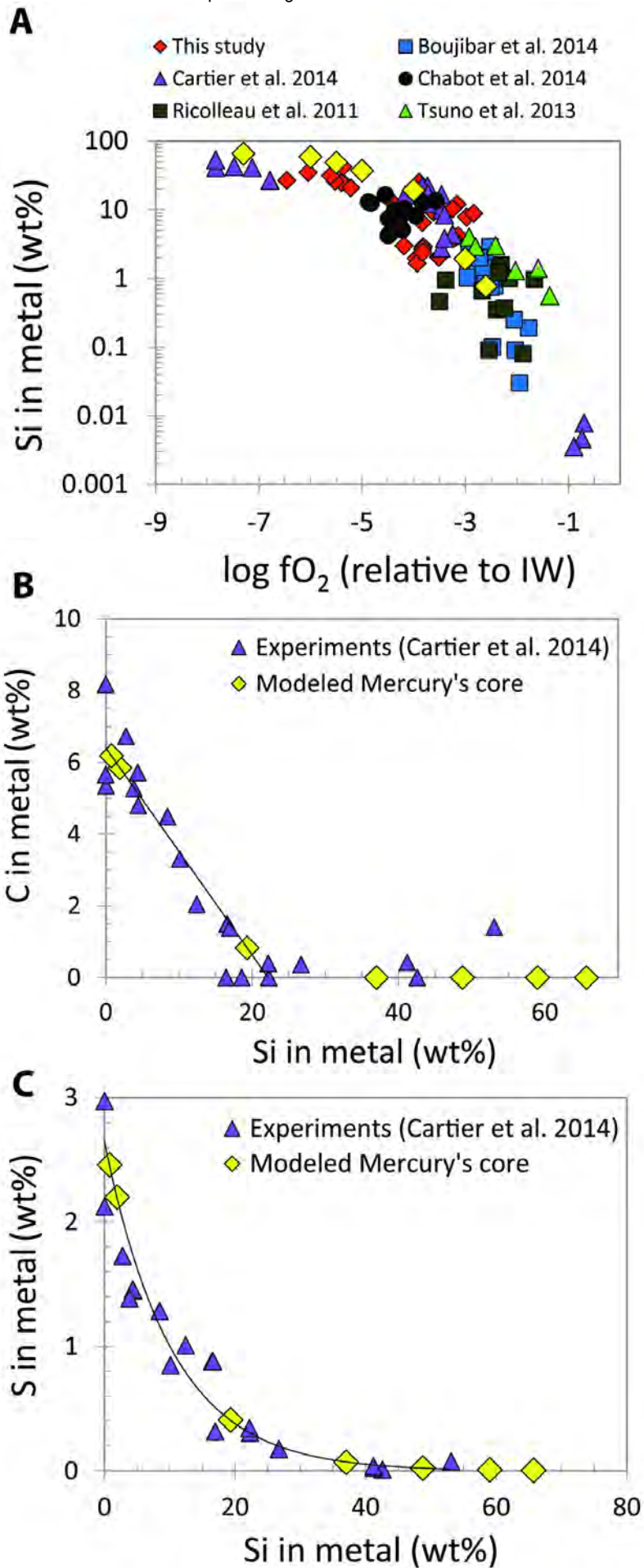e ma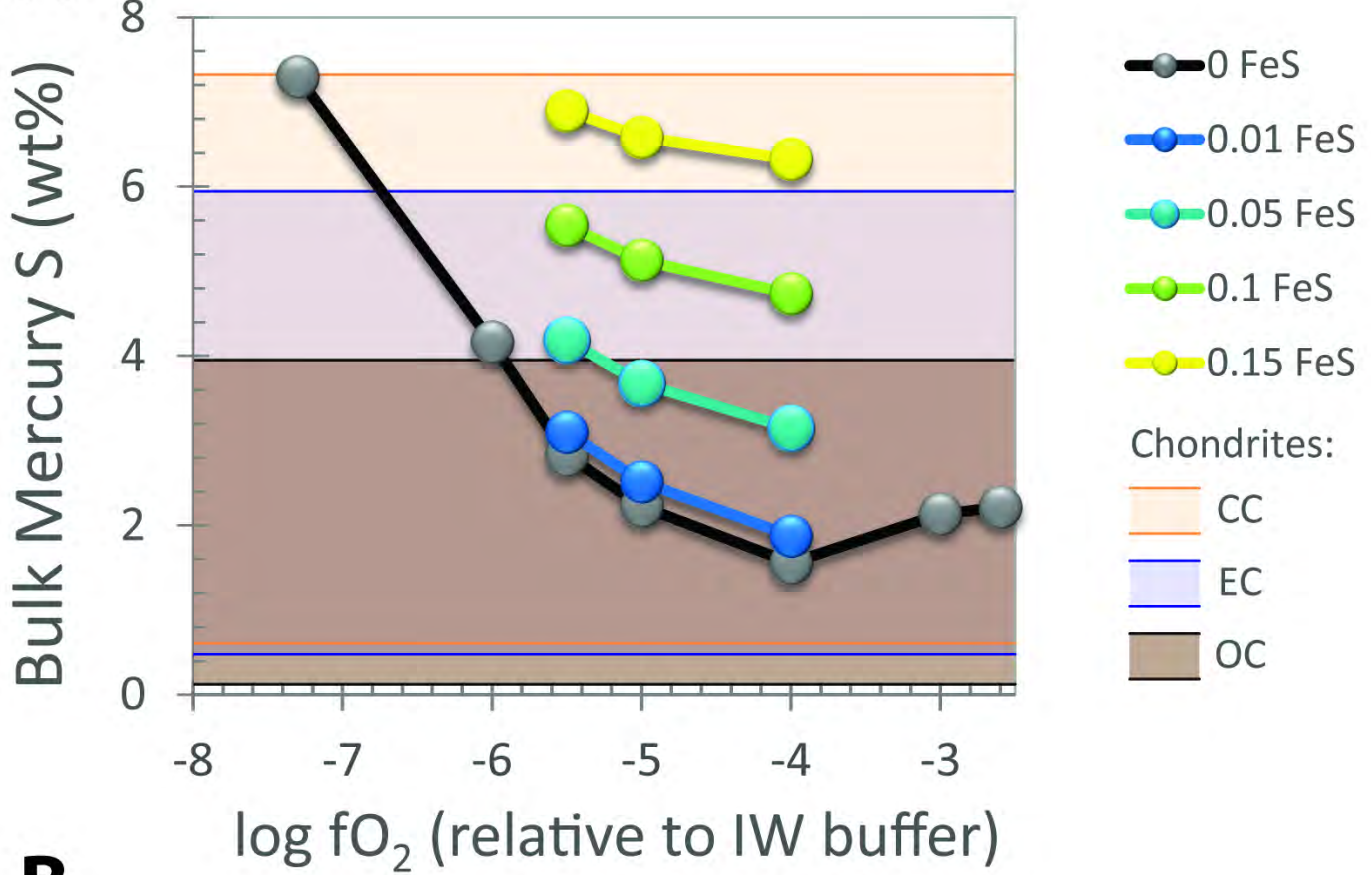ntle, all shown above (see text for more details).